NEUROSCIENCE

Auts2 deletion involves in DG hypoplasia and social recognition deficit: The developmental and neural circuit mechanisms

Jun Li[1]*, Xiaoxuan Sun[1], Yang You[1], Qiongwei Li[1], Chengwen Wei[1], Linnan Zhao[1], Mengwen Sun[1,2], Hu Meng[1], Tian Zhang[1], Weihua Yue[1,3], Lifang Wang[1], Dai Zhang[1,4,5]*

The involvement of genetic risk and the underlying developmental and neural circuit mechanisms in autism-related social deficit are largely unclear. Here, we report that deletion of *AUTS2*, a high-susceptibility gene of ASDs, caused postnatal dentate gyrus (DG) hypoplasia, which was closely relevant to social recognition deficit. Furthermore, a previously unknown mechanism for neural cell migration in postnatal DG development was identified, in which Auts2-related signaling played a vital role as the transcription repressor. Moreover, the supramammillary nucleus (SuM)–DG-CA3 neural circuit was found to be involved in social recognition and affected in *Auts2*-deleted mice due to DG hypoplasia. Correction of DG-CA3 synaptic transmission by using a pharmacological approach or chemo/optogenetic activation of the SuM-DG circuit restored the social recognition deficit in *Auts2*-deleted mice. Our findings demonstrated the vital role of Auts2 in postnatal DG development, and this role was critical for SuM-DG-CA3 neural circuit-mediated social recognition behavior.

INTRODUCTION

Deficiency in social interaction (SI) is one of the core symptoms of autism spectrum disorders (ASDs) (*1*). Accumulated evidence has documented the association of impaired face recognition with the social deficits in patients with autism (*2*–*5*) and the relationship between poor facial recognition and autism-like traits in the general population (*6*–*8*). So far, the involvement of hippocampus (HIP) in face identification and facial recognition has been widely reported (*9*–*12*). In addition, studies on neuroimaging have found that the volume of HIP (*13*, *14*) or dentate gyrus (DG) (*15*) was reduced in individuals with autism compared to typical development controls; another two neuropathological research studies also revealed the DG dysplasia in some cases with autism (*16*, *17*), indicating the possibility that hippocampal dysplasia and/or dysfunction were related to face recognition deficit in autism. However, the involvement of genetic risks of ASDs in hippocampal dysplasia and the underlying molecular and neural circuit mechanisms of impaired social behaviors, including social recognition deficit, are not yet fully understood and needed to be clarified.

An increasing number of studies have reported multiple genetic variations in Autism susceptibility 2 (*AUTS2*) that are associated with autism and related neurodevelopmental disorders (NDDs) (*18*–*25*). However, the influences of *AUTS2* dysfunction on ASD-related social behaviors, as well as underlying developmental and neural circuit mechanisms, are still unclear. In addition, although Auts2 has been implicated in cerebral and cerebellar development (*26*–*29*), its roles in DG development are rarely examined and requiring in-depth study. Here, we revealed a previously unidentified mechanism for neural cell migration in the postnatal DG development, in which Auts2-related signaling played a vital role as the transcription repressor. DG hypoplasia caused by *Auts2* deletion could further lead to the dysfunction of supramammillary nucleus (SuM)–DG-cornus ammonis 3 (CA3) neural circuit, which was involved in the potential pathology of social recognition deficit.

RESULTS

Deletion of *Auts2* in developing forebrain leads to DG hypoplasia and autism-related behaviors in mice

According to a previous study, Auts2 was most abundantly expressed in the HIP and frontal cortex (FC) (*30*). To investigate the critical role of Auts2 in forebrain development, we first detected the temporal expression patterns of Auts2 in the HIP (Fig. 1A) and FC (Fig. 1B). The increasing expression level of Auts2 in the DG at different postnatal days indicated the potential role of this gene in postnatal DG development. As $Auts2^{-/-}$ mice showed embryonic lethality, $Auts2^{fl/fl}$ mice harboring LoxP sites flanking exon 6, which was often found copy number deletion in patients with ASDs and related NDDs (fig. S1A and data S1), were generated and first mated with empty spiracles homeobox 1 (*Emx1*)–Cre mice to specifically disrupt *Auts2* in excitatory neural progenitors in the forebrain (fig. S1B). The reduced expression level of *Auts2* in $Auts2^{fl/fl;Emx1\text{-}Cre}$ mice was verified (Fig. 1, C and D).

The gross morphological analysis showed that the size of DG rather than the cortex or thalamic nuclei was notably reduced in the coronal section of $Auts2^{fl/fl;Emx1\text{-}Cre}$ brain (Fig. 1E and fig. S1, C to G). Further experiments found that the lengths of both suprapyramidal and infrapyramidal blades and the area of the DG were markedly decreased at postnatal day 14 (P14) and P60, although no significance was observed at P4 (Fig. 1, F to H). The length and area of the CA region were not affected. The statistical results were shown in Fig. 1 (I to M). These findings suggested the critical and specific role of Auts2 in postnatal DG development.

[1]Peking University Sixth Hospital, Peking University Institute of Mental Health, NHC Key Laboratory of Mental Health (Peking University), National Clinical Research Center for Mental Disorders (Peking University Sixth Hospital), Beijing, China. [2]Peking-Tsinghua Center for Life Sciences, Peking University, Beijing, China. [3]PKU-IDG/McGovern Institute for Brain Research, Peking University, Beijing, China. [4]Chinese Institute for Brain Research, Beijing, China. [5]Institute for Brain Research and Rehabilitation (IBRR), Guangdong Key Laboratory of Mental Health and Cognitive Science, South China Normal University, Guangzhou, China.
*Corresponding author. Email: daizhang@bjmu.edu.cn (D.Z.); junli1985@bjmu.edu.cn (J.L.)

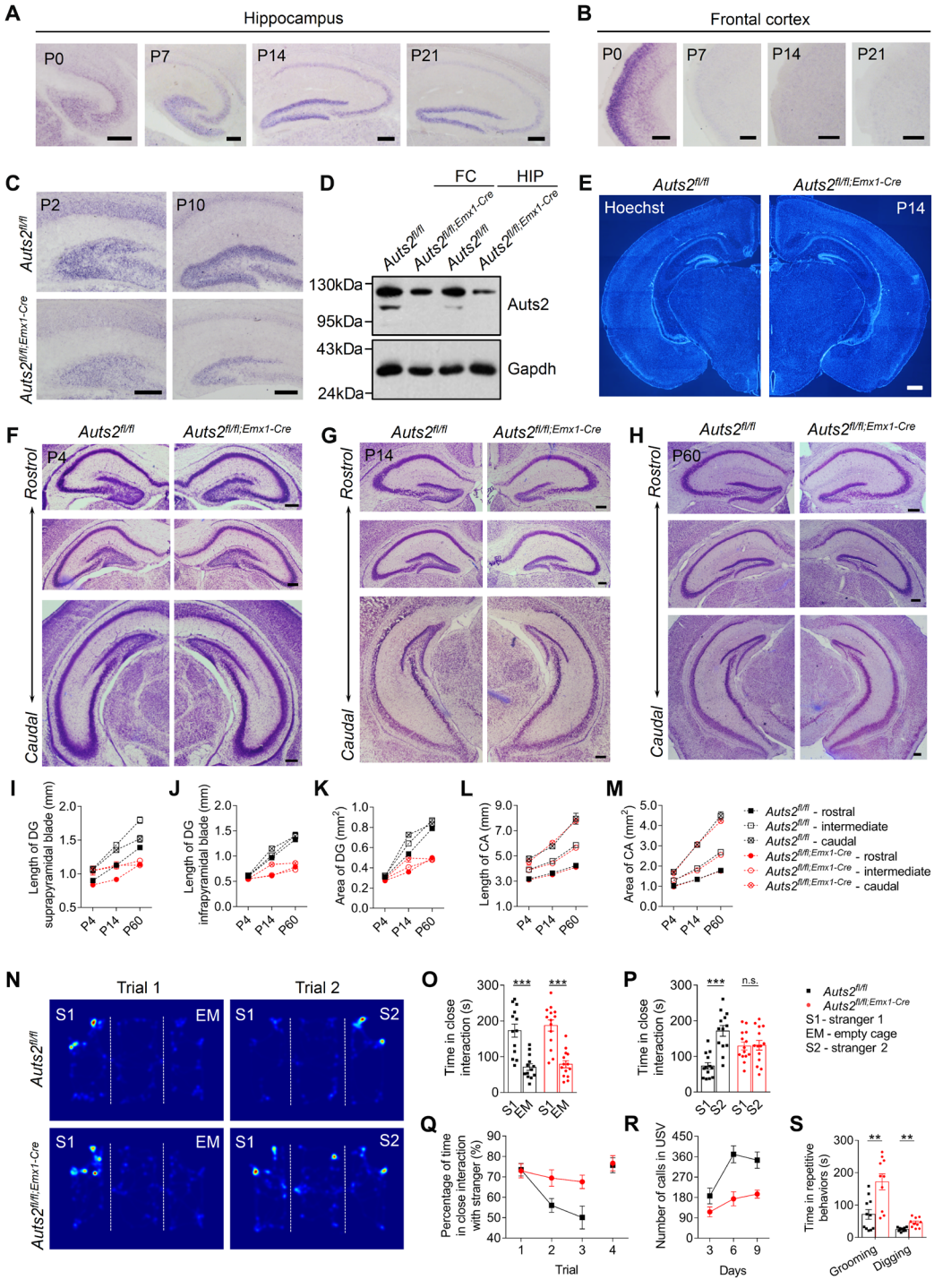

Fig. 1. Deletion of *Auts2* in forebrain excitatory neural progenitors leads to DG hypoplasia and autism-related behaviors. (**A** and **B**) The mRNA expression pattern of *Auts2* in wild-type HIP (A) and FC (B) at different postnatal days. Scale bars, 200 μm. (**C**) *Auts2* mRNA expression in HIP from $Auts2^{fl/fl}$ mice and $Auts2^{fl/fl;Emx1\text{-}Cre}$ mice at P2 and P10. Scale bars, 200 μm. (**D**) *Auts2* protein expression in FC and HIP of $Auts2^{fl/fl}$ mice and $Auts2^{fl/fl;Emx1\text{-}Cre}$ mice at P4. (**E**) P14 coronal sections revealed abnormal morphology of DG in $Auts2^{fl/fl;Emx1\text{-}Cre}$ mice. Scale bar, 500 μm. (**F** to **H**) Morphological changes in postnatal *Auts2*-deleted HIP at P4 (F), P14 (G), and P60 (H). Scale bars, 200 μm. (**I** to **M**) Quantification of the suprapyramidal blade (I) and infrapyramidal blade (J) length, the CA length (L), and the area of DG (K) and CA (M) at P4, P14, and P60; three mice per genotype at each time point. (**N** to **P**) Three-chamber SI test. Representative heatmaps for the different genotypes (N). In trial 1 (S1 versus EM), mice of both genotypes spent more time in close interaction with S1 than EM (O). In trial 2 (S1 versus S2), $Auts2^{fl/fl;Emx1\text{-}Cre}$ mice displayed no preference for the novel social partner S2 [(P) 13 to 14 male mice per genotype]. (**Q**) Social recognition memory test. Male $Auts2^{fl/fl}$ mice, but not $Auts2^{fl/fl;Emx1\text{-}Cre}$ mice, habituated to the same mouse (trials 1 to 3) and dishabituated to a novel mouse (trial 4); 12 male mice per genotype. (**R**) Numbers of ultrasonic vocalizations (USVs) emitted by pups during maternal separation at P3, P6, and P9; 23 to 24 pups per genotype. (**S**) Increased stereotyped grooming and digging behaviors in male $Auts2^{fl/fl;Emx1\text{-}Cre}$ mice; 10 to 11 male mice per genotype. Data were shown as means ± SEM. Two-tailed Student's *t* test and two-way analysis of variance (ANOVA). $^{**}P < 0.01$ and $^{***}P < 0.001$; n.s., no significance.

Auts2$^{fl/fl;Emx1\text{-}Cre}$ mice looked healthy and had a normal body weight (fig. S1H). To study the potential effect of *Auts2* deletion on ASD-related behaviors, we conducted a battery of tests. The three-chamber SI test in male *Auts2*$^{fl/fl;Emx1\text{-}Cre}$ mice (Fig. 1, N to P) showed normal voluntary initiation with a stranger mouse [stranger 1 (S1); Fig. 1O] in stage 1 but impaired ability to discriminate S1 and stranger 2 (S2; Fig. 1P) in stage 2. Additional four-trial social recognition assay found that the male *Auts2*$^{fl/fl;Emx1\text{-}Cre}$ mice appeared impairment of habituation to S1 and dishabituation to S2 (Fig. 1Q), confirming that Auts2 was necessary for social recognition memory. However, both the odor and novel object recognition behaviors in male *Auts2*$^{fl/fl;Emx1\text{-}Cre}$ mice were normal (fig. S1, I and J), which indicated that social recognition instead of odor or object novelty recognition was affected. Similarly, the female *Auts2*$^{fl/fl;Emx1\text{-}Cre}$ mice also showed deficit in social novelty recognition (fig. S1, K and L).

In addition, the number of isolation-induced ultrasonic vocalizations (USVs) emitted by *Auts2*$^{fl/fl;Emx1\text{-}Cre}$ pups was less than that emitted by their control littermates at different postnatal days (Fig. 1R). The excessive grooming and digging behaviors were also observed in both male and female *Auts2*$^{fl/fl;Emx1\text{-}Cre}$ mice (Fig. 1S and fig. S1M). These results indicated the abnormal social communication and increased stereotyped behaviors in *Auts2*-deleted mice. Nevertheless, the male *Auts2*$^{fl/fl;Emx1\text{-}Cre}$ mice showed normal spatial learning and memory (fig. S1, N and O), contextual fear memory (fig. S1, P and Q), spontaneous alternation (fig. S1R), and locomotor activity (fig. S1S). The anxiety-like behaviors (fig. S1, T to V) and sensory gating test (fig. S1W) also showed no difference between the two genotypes.

Auts2 deletion–induced DG hypoplasia is closely related to social recognition deficit in mice

As Auts2 is highly expressed in postmitotic granular cells (GCs) (*30*), mice with neuronal helix-loop-helix protein (*Nex*)–Cre–mediated, proopiomelanocortin (*Pomc*)–Cre–mediated, and calcium/calmodulin-dependent protein kinase II (*CaMKII*)–Cre–mediated *Auts2* deletion were further generated, in which *Auts2* was conditionally disrupted at different developmental stages and in distinct forebrain areas (fig. S2, A to D). We found that *Auts2*$^{fl/fl;Nex\text{-}Cre}$ mice and *Auts2*$^{fl/fl;Pomc\text{-}Cre}$ mice also appeared DG hypoplasia at P14 (Fig. 2, A and B, and fig. S2, E and F), which was consistent with the morphological phenotype observed in *Auts2*$^{fl/fl;Emx1\text{-}Cre}$ mice. However, both the *Auts2*$^{fl/fl;CaMKII\text{-}Cre}$ mice (Fig. 2C and fig. S2G) and mice with virus-mediated *Auts2* deletion in GCs at P14 (Fig. 2D and fig. S2, H and I) showed normal morphology of DG. These results further verified that the function of Auts2 in postmitotic GCs was critical for DG development at early postnatal stage.

To further investigate the potential association of *Auts2* deletion–mediated DG hypoplasia with autism-related abnormal core behaviors, we first conducted the three-chamber SI test in the above mouse lines (Fig. 2, E to H). We found that social recognition deficit was apparent in *Auts2*$^{fl/fl;Nex\text{-}Cre}$ mice (Fig. 2E) and *Auts2*$^{fl/fl;Pomc\text{-}Cre}$ mice (Fig. 2F), but not *Auts2*$^{fl/fl;CaMKII\text{-}Cre}$ mice (Fig. 2G) or *Auts2*$^{fl/fl}$ mice injected with virus containing *CaMKII*-driven Cre (Fig. 2H). In addition, although the USV showed no difference compared to controls (fig. S2J), the excessive grooming behavior was observed in *Auts2*$^{fl/fl;Nex\text{-}Cre}$ mice (fig. S2K). Both the USV and stereotyped behaviors represented normal in *Auts2*$^{fl/fl;Pomc\text{-}Cre}$ mice (fig. S2, L and M). These results suggested a close association between *Auts2* deletion–induced DG hypoplasia and social recognition deficit.

Auts2 deletion involves in sustained SPZ and impaired SGZ formation in postnatal DG through regulation of NSC/IPC migration

The cell composition analysis revealed that the numbers of brain lipid binding protein-positive (BLBP$^+$) neural stem cells (NSCs), T-box transcription factor T-brain 2-positive (Tbr2$^+$) intermediate precursor cells (IPCs), calretinin$^+$ (immature)/NeuN$^+$ (mature) postmitotic neurons, and glial fibrillary acidic protein-positive (GFAP$^+$) astrocytes were significantly reduced at P14 (Fig. 3A), while the relative percentages of these cell types based on total DG cell number showed no significant difference in *Auts2*$^{fl/fl;Emx1\text{-}Cre}$ mice compared to controls (fig. S3A). These results suggested that the cell number rather than cellular compartment populations was affected by *Auts2* deletion.

The DG hypoplasia might be due to the abnormalities of several highly regulated processes including cell proliferation, differentiation, apoptosis, and migration. The effect of apoptosis was first precluded by the cleaved caspase-3 staining (Fig. 3B). The number of proliferative cells in the DG was found significantly reduced in *Auts2*$^{fl/fl;Emx1\text{-}Cre}$ mice at P7 (Fig. 3C and fig. S3B), which was attributed to significantly less number of Ki67$^+$ cells in the regions of granular cell layer (GCL) and hilus rather than the molecular cell layer (MCL) (Fig. 3C). Similarly, the cell cycle exit assay also showed a region-specific difference between *Auts2*$^{fl/fl}$ mice and *Auts2*$^{fl/fl;Emx1\text{-}Cre}$ mice (Fig. 3D), suggesting that the damaged cell migration might be involved.

Furthermore, we observed ectopic Tbr2$^+$ cells in the GCL of *Auts2*$^{fl/fl;Emx1\text{-}Cre}$ mice at P14 (Fig. 3A), and thus, the IPC migration at different postnatal stages was examined (Fig. 3, E to G). We found a similar distribution pattern of Tbr2$^+$ IPCs in both genotypes at P2 (Fig. 3E), which indicated the normal tangential migration of NSCs/IPCs along the dentate migratory stream and subpial zone (SPZ) formation in *Auts2*$^{fl/fl;Emx1\text{-}Cre}$ mice. However, the proportion of Tbr2$^+$ cells that radially migrated into the GCL and hilus was significantly less in the dorsal half of the DG compared to controls, accompanied by many Tbr2$^+$ cells packed in the SPZ of *Auts2*$^{fl/fl;Emx1\text{-}Cre}$ mice at P5 (Fig. 3F) and P7 (Fig. 3G), suggesting that the dentate neurogenic niche failed to undergo the SPZ–to–subgranular zone (SGZ) transition. This further resulted in an impaired SGZ formation and decreased neurogenesis in SGZ of *Auts2*$^{fl/fl;Emx1\text{-}Cre}$ mice at P14 (Fig. 3H and fig. S3C) and P60 (fig. S3D), while neurogenesis in the subventricular zone was normal (fig. S3E). Moreover, the impaired Tbr2$^+$ IPC migration from SPZ to SGZ was also observed in both *Auts2*$^{fl/fl;Nex\text{-}Cre}$ mice and *Auts2*$^{fl/fl;Pomc\text{-}Cre}$ mice at P7 (Fig. 3, I and J), although the phenotype was milder than that in *Auts2*$^{fl/fl;Emx1\text{-}Cre}$ mice, indicating both cell-autonomous and non–cell-autonomous manners might be involved in the *Auts2* deletion–mediated SPZ to SGZ transition deficit.

Nevertheless, *Auts2*-deleted cells showed normal migration from the dentate neuroepithelium to the developing DG at the embryonic stage (fig. S3, F and G). The proliferative ability of NSCs and IPCs in the postnatal DG was further verified and found that their proliferation rates were only significantly decreased at P7 but not at P14 (Fig. 3, K and L), suggesting that the decreased proliferative ability of NSCs and IPCs at P7 might be resulted from their deficits in migration from the SPZ to the SGZ. Neurogenesis and gliogenesis in the postnatal DG also showed no significant difference between the two genotypes (fig. S3, H and I). The secondary

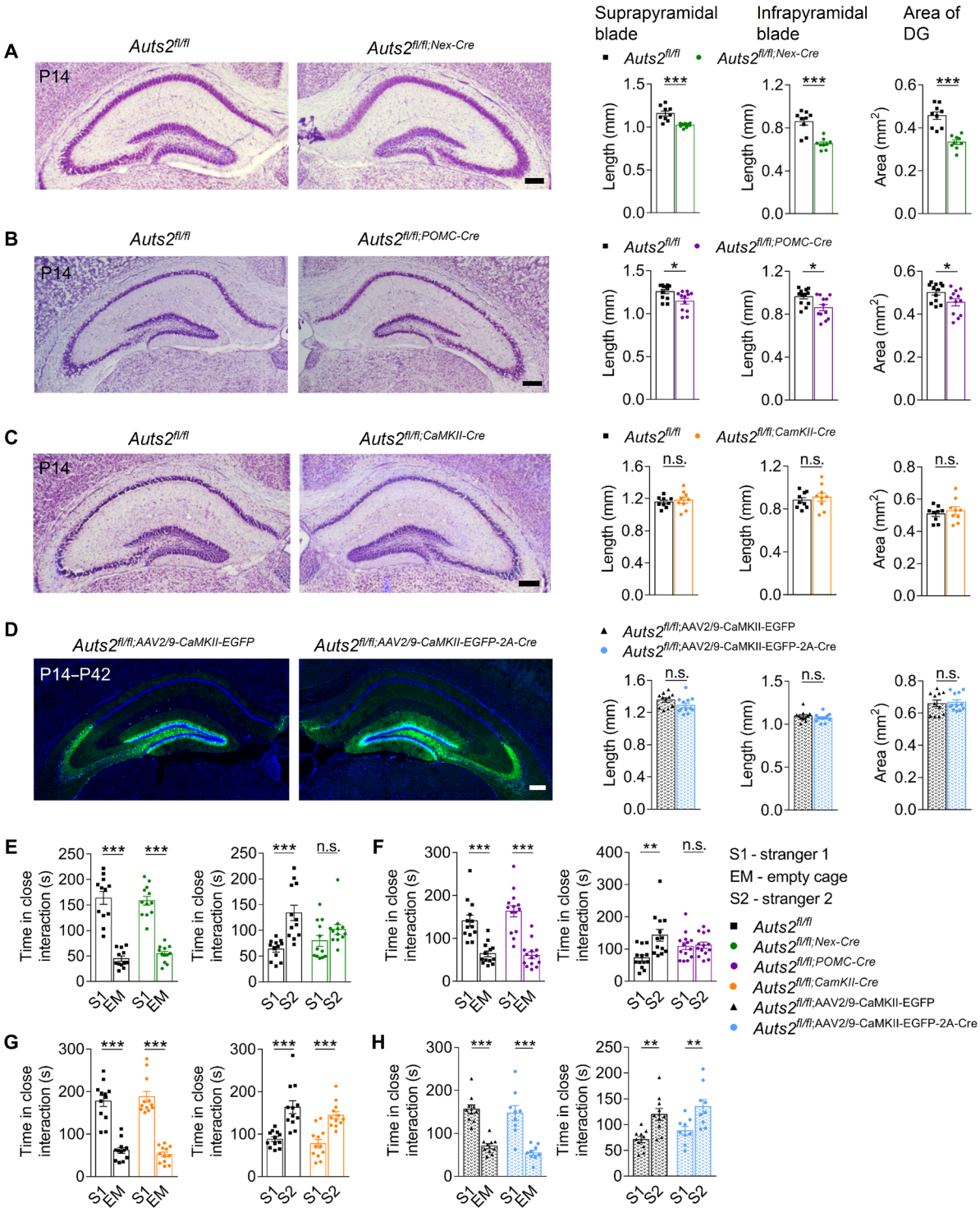

Fig. 2. *Auts2* deletion–induced DG hypoplasia is closely related to social recognition deficit in mice. (**A** to **D**) Morphological analysis of the postnatal *Auts2*-deleted HIP. Representative images showed Nissl staining of coronal HIP sections from *Auts2*$^{fl/fl;Nex\text{-}Cre}$ mice (A), *Auts2*$^{fl/fl;Pomc\text{-}Cre}$ mice (B), and *Auts2*$^{fl/fl;CaMKII\text{-}Cre}$ mice (C) compared to *Auts2*$^{fl/fl}$ mice at P14 and HIP sections from P42 *Auts2*$^{fl/fl}$ mice with AAV2/9-CaMKII-EGFP-2A-Cre or vehicle injection in the DG at P14 (D). Scale bars, 200 μm. Quantification of the length of the suprapyramidal and infrapyramidal blades and area of the DG in different mouse lines, respectively; 9 to 12 slices from three to four mice per genotype. (**E** to **H**) Three-chamber SI test. In the sociability trial (S1 versus EM), all of the above mouse lines spent more time in close interaction with S1 than EM. In the social novelty preference trial (S1 versus S2), the male *Auts2*$^{fl/fl;Nex\text{-}Cre}$ mice (E) and *Auts2*$^{fl/fl;Pomc\text{-}Cre}$ mice (F), but not *Auts2*$^{fl/fl;CaMKII\text{-}Cre}$ mice (G) or *Auts2*$^{fl/fl}$ mice with AAV-mediated Auts2 knockout in the mature DG (H), showed a decreased preference for the novel social partner S2; 9 to 13 male mice per genotype. Data were shown as means ± SEM. Two-tailed Student's *t* test. **P* < 0.05, ***P* < 0.01, and ****P* < 0.001.

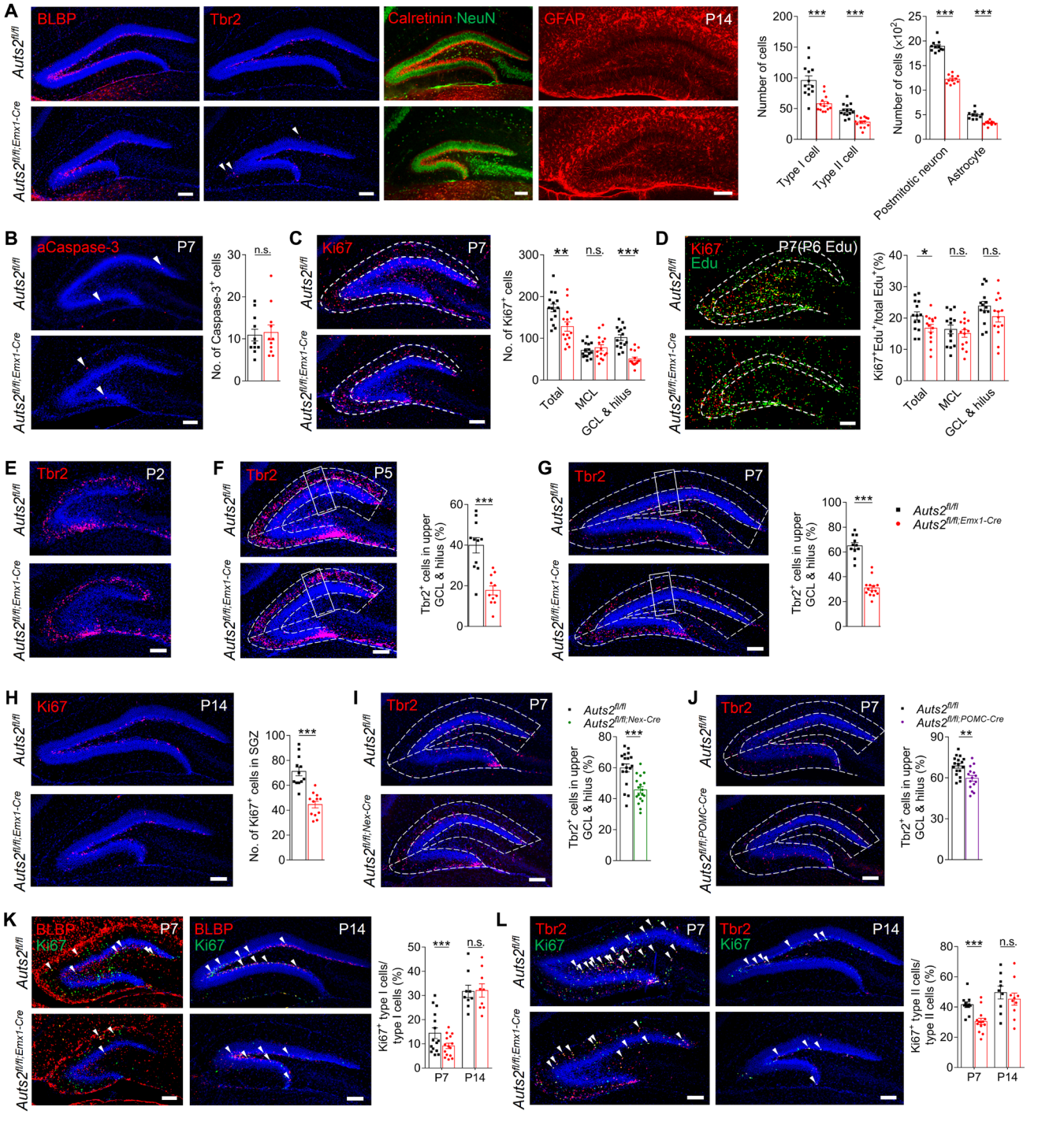

Fig. 3. *Auts2* deletion involves in sustained subpial neurogenic zone and impaired SGZ formation in postnatal DG through regulation of NSC/IPC migration. (**A**) The cell numbers of each type were calculated at P14; 11 to 15 slices from three to four mice per genotype. (**B**) Cell death was evaluated by cleaved caspase-3 immunostaining at P7; 11 slices from three mice per genotype. (**C**) The proliferative rate was evaluated by Ki67 staining at P7. (**D**) Cell cycle re-entry was analyzed by Ki67 and EdU double labeling at P7 24 hour after EdU injection; 14 to 15 slices from four mice per genotype. MCL, molecular cell layer; GCL, granular cell layer. (**E** to **G**) Impaired IPC migration in *Auts2*$^{fl/fl;Emx1\text{-}Cre}$ mice. IPC migration was evaluated by Tbr2 labeling at P2 (E), P5 (F), and P7 (G). The percentage of Tbr2$^+$ cells in the area including the dorsal half of GCL and hilus region was calculated at P5 (F) and P7 (G); 11 to 14 slices from three to four mice per genotype. (**H**) Shrinking of SGZ and a decrease of neurogenesis in *Auts2*-deleted DG at P14; 12 to 13 slices from three mice per genotype. (**I** and **J**) IPC migration in *Auts2*$^{fl/fl;Nex\text{-}Cre}$ mice (I) and *Auts2*$^{fl/fl;Pomc\text{-}Cre}$ mice (J) was evaluated by Tbr2 labeling at P7; 15 to 20 slices from three to four mice per genotype. (**K** and **L**) The proliferation rate of NSCs and IPCs in the developmental DG was assessed by co-immunostaining with Ki67 and BLBP (K) or Tbr2 (L). The ratio of Ki67$^+$ (green) and BLBP$^+$ [red (K)]/Tbr2$^+$ [red (L)] double-labeled cells divided by the total number of BLBP$^+$ (K)/Tbr2$^+$ (L) cells was calculated at P7 and P14; 9 to 15 slices from three to four mice per genotype. MZ, marginal zone. Scale bars, 100 μm. Data were shown as means ± SEM. Two-tailed Student's *t* test. **P* < 0.05, ***P* < 0.01, and ****P* < 0.001.

radial glial scaffolds were well established in both genotypes at P7 (fig. S3J) and P14 (fig. S3K).

Auts2-Ctip2-NuRD complex represses *Ptgds* transcription and involves in the NSC/IPC migration from SPZ to SGZ

To explore the underlying molecular mechanism of *Auts2* deletion–mediated DG hypoplasia, we first conducted the microarray transcriptome analysis and found that the numbers of up-regulated and down-regulated genes in the DGs of $Auts2^{fl/fl;Emx1\text{-}Cre}$ and control mice were comparable (fig. S4, A to F). Among the common top hit genes, we focused on prostaglandin D2 synthase (*Ptgds*) due to its preferential expression pattern in the brain and potential function in neurodevelopment. We verified its elevated expression in the DG of $Auts2^{fl/fl;Emx1\text{-}Cre}$ mice (Fig. 4, A to C), as well as $Auts2^{fl/fl;Nex\text{-}Cre}$ mice (fig. S4G) and $Auts2^{fl/fl;Pomc\text{-}Cre}$ mice (fig. S4H) at P4. These results indicated the ectopic up-regulation of Ptgds in the *Auts2*-deleted GCs.

The effect of Ptgds up-regulation on postnatal DG development was further confirmed by virus-mediated overexpression in early postmitotic GCs (fig. S4I). We found that the mice with Ptgds overexpression showed abnormal $Tbr2^+$ IPC migration from SPZ to SGZ (Fig. 4D) and DG hypoplasia at P7 (Fig. 4E), as well as abnormal SGZ formation at P14 (Fig. 4F), which mimicked the phenotypes of *Emx1*-Cre–, *Nex*-Cre–, or *Pomc*-Cre–mediated *Auts2* deletion in the DG. In addition, social recognition deficit was also observed in mice with Ptgds overexpression (Fig. 4G). These results demonstrated that the appropriate level of Ptgds expression in early postmitotic GCs was important for Auts2-dependent postnatal DG development.

COUP-TF-interacting protein 2 (Ctip2), known as a transcription repressor that is regulated by the Nucleosome Remodeling and Deacetylase (NuRD) complex (*31*), was reported its involvement in the DG formation (*32*) and colocalization with Auts2 during neurodevelopment (*27*). In the present study, we identified several target genes including Ptgds coregulated by Ctip2 and Auts2 (fig. S4C), indicating the potential role of Ctip2-NuRD complex in the up-regulation of Ptgds upon Auts2 absence. Metastasis associated 1 (MTA1), a member of the NuRD complex, was reported to directly bind to CTIP2 in T lymphocytes (*31*). Here, we found that CTIP2 interacted with AUTS2 (Fig. 4H) and MTA1 (Fig. 4I). However, AUTS2 showed no interaction with MTA1 unless CTIP2 was cotransfected (Fig. 4, J and K), suggesting that CTIP2 could mediate the interaction between AUTS2 and MTA1. The protein-protein interactions in vivo was further explored and found that Ctip2 interacted with both Mta1 and Auts2 in the control DG; however, *Auts2* deletion significantly weakened the interaction of Mta1 with Ctip2 (Fig. 4L).

The luciferase assay revealed that overexpressed CTIP2 rather than AUTS2 could repress PTGDS promoter–mediated luciferase expression in vitro. However, AUTS2 could significantly increase the repressive ability of CTIP2 (Fig. 4M). Furthermore, the chromatin immunoprecipitation (ChIP) assay demonstrated that both Ctip2 and histone deacetylase 2 (Hdac2), one of the two histone deacetylases in NuRD complex, could directly bind to the promoter of Ptgds in the control DG at P4 (Fig. 4N). Auts2 deficiency largely decreased the binding of Hdac2, but not Ctip2, to the Ptgds promoter (Fig. 4, O and P). These results indicated that Auts2 was required for Ctip2-mediated repression of Ptgds by recruiting NuRD complex to the promoter in postmitotic GCs, which was involved in NSC/IPC migration in early postnatal DG. The ectopic expression of Ptgds in GCs led to abnormal SPZ to SGZ transition and DG hypoplasia in *Auts2*-deleted mice (Fig. 4Q).

Decreased DG-CA3 synaptic transmission caused by DG hypoplasia involves in social recognition deficit

To reveal the consequence of DG hypoplasia on the hippocampal neural network, we first determined the morphological and electrophysiological features of GCs. The width of the calbindin-labeled main bundle (MB), which was used to represent the number of GC axon terminals, was significantly decreased in $Auts2^{fl/fl;Emx1\text{-}Cre}$ mice (Fig. 5A), although the length of the MB was not affected. The dendritic length and complexity of GCs were also not influenced by *Auts2* deletion (Fig. 5A and fig. S5A). In addition, the frequency and amplitude of miniature excitatory postsynaptic currents (mEPSCs) and miniature inhibitory postsynaptic currents (mIPSCs) recorded in GCs showed normal in $Auts2^{fl/fl;Emx1\text{-}Cre}$ mice (fig. S5B). The action potential of GCs also appeared no significant difference between the two genotypes (fig. S5C).

To further determine DG-CA3 neurotransmission and the excitability of pyramidal neurons (PNs) in CA3, we recorded the action potentials, mEPSCs, and mIPSCs (Fig. 5, B to D). We found that the mEPSC frequency instead of amplitude was significantly decreased in $Auts2^{fl/fl;Emx1\text{-}Cre}$ PNs, while the frequency of action potentials and both the frequency and amplitude of mIPSCs were not affected (Fig. 5, B to D). Moreover, the DG-CA3 paired-pulse ratio showed no significant difference between the two genotypes (fig. S5D). These results indicated that presynaptic-dependent DG-CA3 synaptic transmission, rather than short-term plasticity, was impaired in $Auts2^{fl/fl;Emx1\text{-}Cre}$ mice.

To explore the involvement of DG-CA3 circuit in social recognition behavior, we overexpressed human Gi-coupled M4 muscarinic receptor (hM4Di) in mature wild-type GCs (Fig. 5, E and F) to inhibit the neuronal activity (fig. S5E) and found that the frequency of mEPSCs recorded in CA3 PNs was significantly reduced (Fig. 5G). Impaired social recognition, but not novel object recognition, was observed in the hM4Di group compared to the control after clozapine N-oxide (CNO) administration (Fig. 5H and fig. S5F). Furthermore, administration of α-methyl-4-carboxyphenylglycine (MCPG), which targeted the presynaptic metabotropic glutamate receptor (mGluR) of DG-CA3 mossy fiber as an antagonist, could block the presynaptic inhibition of transmitter release and thus facilitate the DG-CA3 synaptic transmission (Fig. 5I). Injection of MCPG into the bilateral DG-CA3 terminals of $Auts2^{fl/fl;Emx1\text{-}Cre}$ mice largely restored the social recognition deficit (Fig. 5, J to L), suggesting that decreased DG-CA3 synaptic transmission caused by DG hypoplasia was involved in social recognition deficit.

Modulation of SuM-DG circuit activity regulates DG-CA3 synaptic transmission and social recognition behavior

To investigate the neural circuit mechanism of DG hypoplasia involved in ASD-related social recognition deficit at the mesoscopic level, we first evaluated the neuronal activity in HIP and detected more number of $c\text{-}Fos^+$ cells in the GCL of DG and PN layer of CA3 in $Auts2^{fl/fl}$ mice than that in $Auts2^{fl/fl;Emx1\text{-}Cre}$ mice after the SI test (Fig. 6, A to C). In contrast, the DG-CA3 circuit appeared no significant activation in $Auts2^{fl/fl}$ mice after the novel object recognition test (fig. S6A). Then, the potential roles of DG-related upstream neural circuits were investigated when provoked by social recognition in mice by retrograde virus-mediated trace and labeling (Fig. 6D). The labeled enhanced green fluorescent protein-positive ($EGFP^+$) cells were mainly observed in three first-order projection areas: the SuM (Fig. 6E), lateral entorhinal cortex

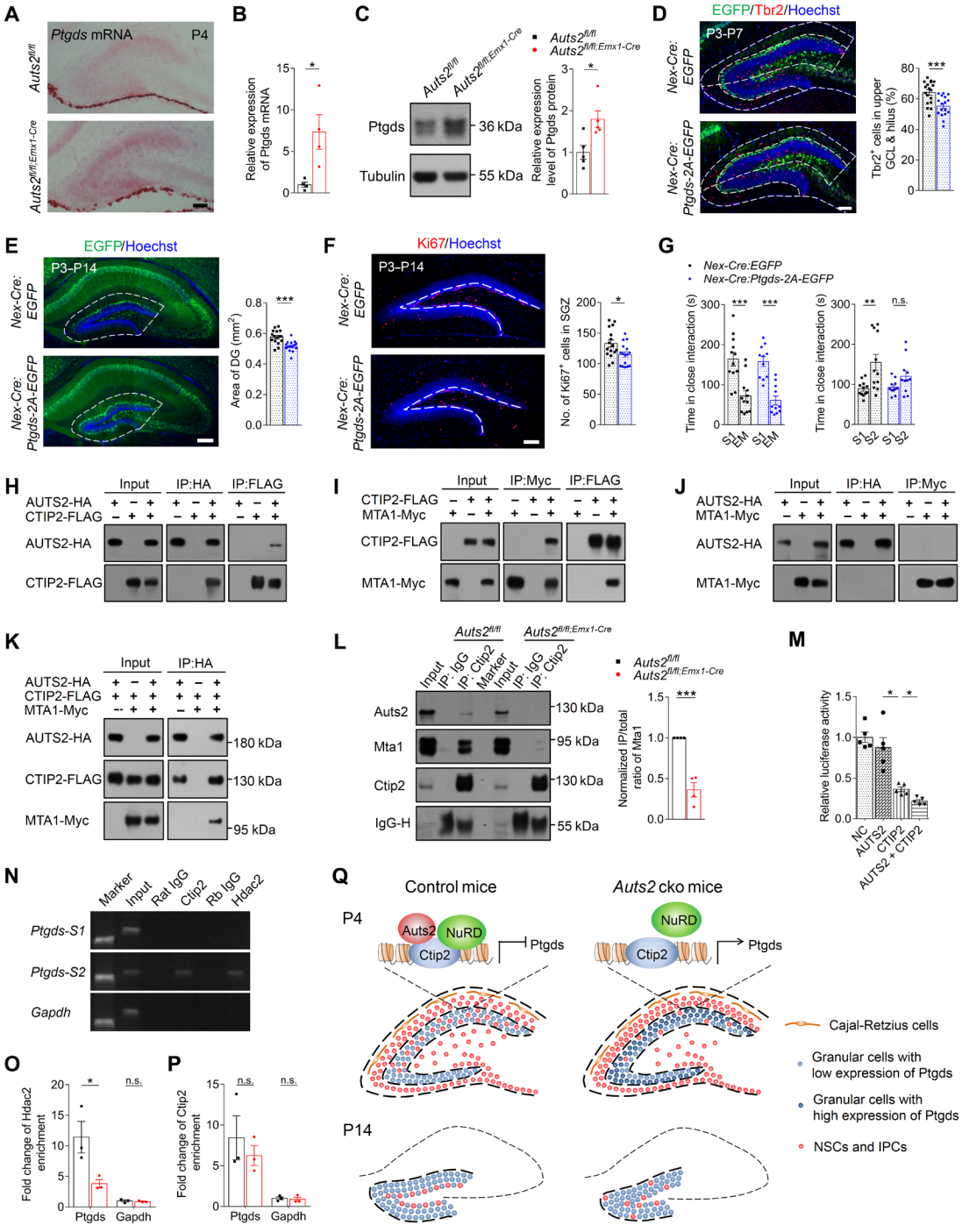

Fig. 4. Ptgds transcription modulated by the Auts2-Ctip2-NuRD complex in postmitotic GCs is involved in NSC/IPC migration from SPZ to SGZ. (**A** and **B**) Detection of Ptgds mRNA expression in DG by RNAscope [(A) scale bar, 100 μm] and quantitative real-time polymerase chain reaction (PCR) [(B) four mice per genotype). (**C**) Detection of Ptgds protein expression in DG; five mice per genotype. (**D** to **F**) *Nex*-Cre mice were injected with AAV2/9-DIO-Ptgds-2A-EGFP or AAV2/9-DIO-EGFP in DG at P3 for assessment of IPC migration [(D) scale bar, 100 μm], the area of DG [(E) scale bar, 200 μm], and SGZ proliferation [(F) scale bar, 100 μm]; 15 to 18 slices from four mice per genotype. (**G**). Three-chamber SI test. *Nex*-Cre mice with Ptgds overexpression showed a decreased preference for S2 over S1; 11 to 12 mice per group. (**H** to **K**) Pairwise interactions among AUTS2, CTIP2, and MTA1. The lysates of HEK293T cells were immunoprecipitated, and the precipitates were analyzed with antibodies against HA, FLAG, and Myc. (**L**) DG lysates from *Auts2*$^{fl/fl}$ mice and *Auts2*$^{fl/fl;\ Emx1\text{-}Cre}$ mice at P4 were immunoprecipitated with antibody against Ctip2. The precipitates were analyzed with antibodies against Auts2, Mta1, and Ctip2; four mice per genotype. (**M**) Transcriptional activity was detected by using dual luciferase assay from five independent tests. (**N** to **P**) Chromatin immunoprecipitation (ChIP) assay. DG extracts at P4 were immunoprecipitated with antibodies against Ctip2 and Hdac2 to obtain the precipitates. The segments of Ptgds promoter were detected by PCR and agarose gel electrophoresis with Gapdh as control (N). The fold change of Ptgds promoter segment 2 immunoprecipitated by Hdac2 (O) and Ctip2 (P) antibodies was analyzed by quantitative real-time PCR; three mice per genotype. (**Q**) Proposed model for Ptgds transcription modulated by the Auts2-Ctip2-NuRD complex in postmitotic GCs. cko, conditional knockout. Data were shown as means ± SEM. Two-tailed Student's *t* test. **P* < 0.05, ***P* < 0.01, and ****P* < 0.001.

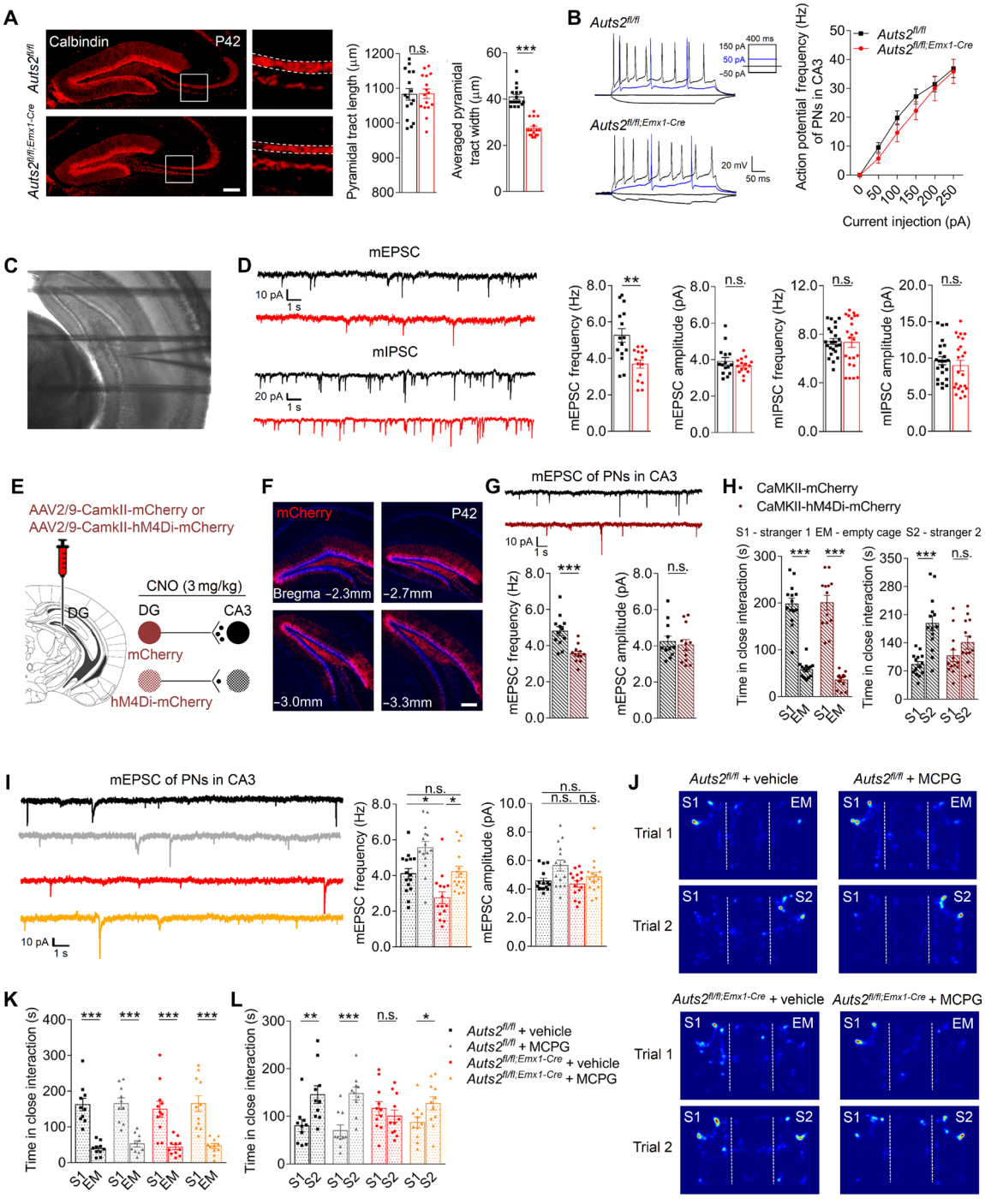

Fig. 5. Decreased synaptic transmission in DG-CA3 neural circuit caused by DG hypoplasia is involved in social recognition deficit. (**A**) Morphological analysis of DG-CA3 axon projection by calbindin immunostaining at P42; scale bar, 200 μm; 16 slices from three mice per genotype. (**B**) The action potentials fired during 400-ms incremental current injections (from −50 to 150 pA; blue trace represented 50 pA; see inset) were recorded in CA3 PNs and action potential frequency was calculated; 14 to 16 cells from six mice per genotype. (**C** and **D**) Decreased mEPSC frequency in CA3 PNs of *Auts2*$^{fl/fl;Emx1\text{-}Cre}$ mice. Representative image represented a whole-cell patch clamp assay (C). Miniature excitatory and inhibitory postsynaptic currents (mEPSCs and mIPSCs) were recorded in CA3 PNs [(D) mEPSCs: 15 cells from three mice per genotype; mIPSCs: 23 cells from five mice per genotype]. (**E** to **H**) Inhibition of DG excitability led to decreased mEPSC frequency in CA3 PNs and social recognition deficit in mice. Diagram of virus injection in DG (E). mCherry expressed in different coronal sections of DG [(F) scale bar, 200 μm]. Example traces and pooled data showed decreased mEPSC frequency in CA3 PNs [(G) 12 cells from three mice per genotype]. Mice with hM4Di overexpression in DG showed social recognition deficit in SI test 30 min after CNO intraperitoneal injection [(H) 13 to 14 male mice per group]. (**I**) The metabotropic glutamate receptor (mGluR) antagonist MCPG reversed the decreased mEPSC frequency in CA3 PNs of *Auts2*$^{fl/fl;Emx1\text{-}Cre}$ mice; 15 cells from three mice per group. (**J** to **L**) Three-chamber SI test. The heatmap represented different genotypes and treatment groups (J). MCPG showed no effect on sociability (K) but reversed the impairment of social novelty preference in male *Auts2*$^{fl/fl;Emx1\text{-}Cre}$ mice [(L) 10 to 11 male mice per genotype]. Data were shown as means ± SEM. Two-tailed Student's *t* test. **P* < 0.05, ***P* < 0.01, and ****P* < 0.001.

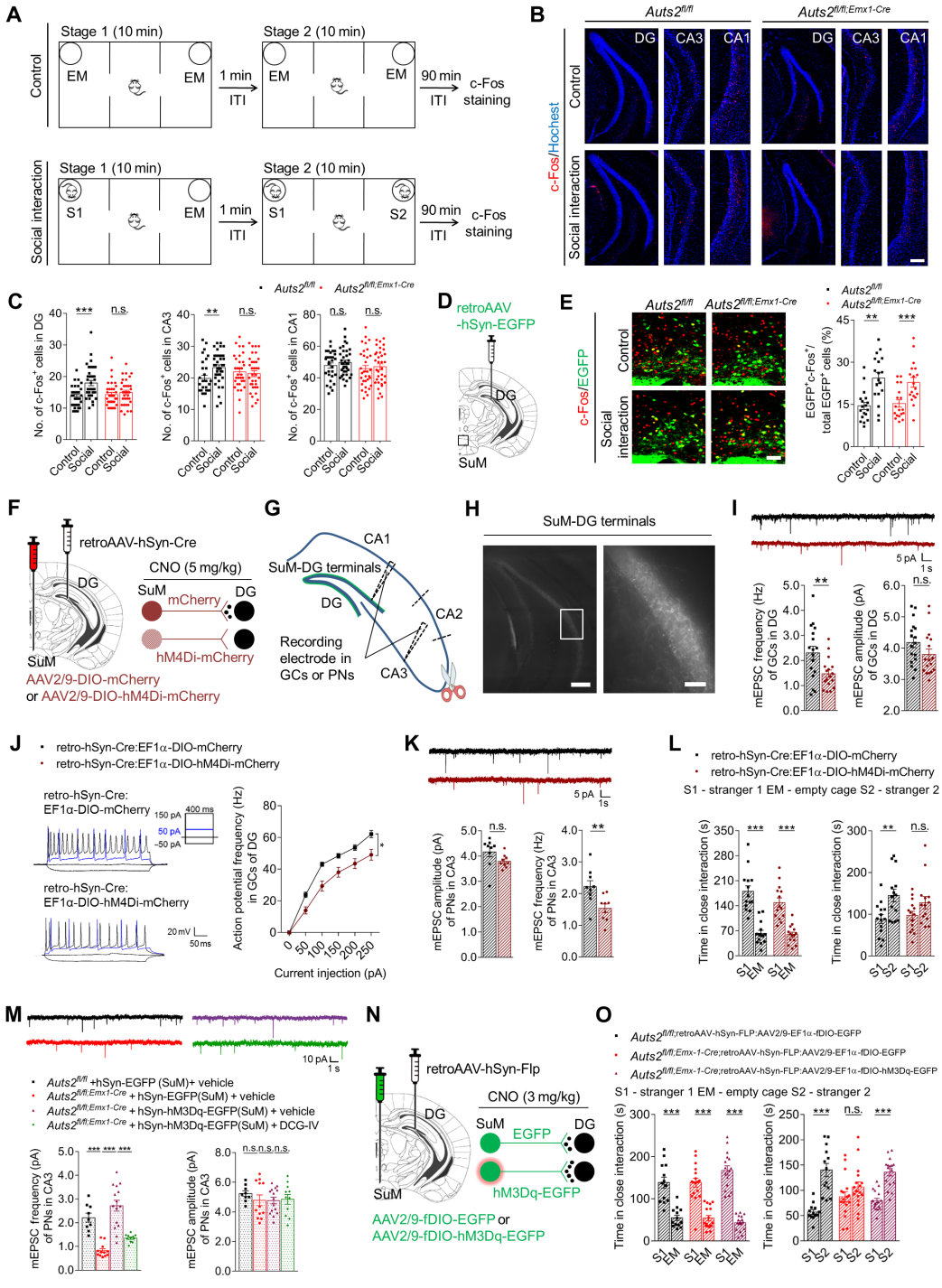

Fig. 6. Activity modulation of SuM-DG circuit regulates DG-CA3 synaptic transmission and social recognition behavior. (**A** to **C**) Neuronal activity analysis in HIP after SI test. A diagram showed the paradigm of c-Fos staining (A). Representative immunostaining of c-Fos$^+$ cells; scale bar, 200 μm (B). The c-Fos$^+$ cell number in HIP was calculated; 30 to 37 slices from four male mice per genotype (C). (**D** and **E**) Activity of DG-projecting SuM neurons was analyzed after SI test. Diagram of retroAAV-hSyn-EGFP injection in DG (D). The activation of SuM EGFP$^+$ cells was evaluated by c-Fos immunostaining (scale bar, 50 μm); 18 slices from four mice per genotype (E). (**F** to **L**) Inhibition of SuM-DG circuit led to decreased GC excitability, reduced DG-CA3 neural transmission, and social recognition deficits. Diagrams showed virus injection in DG and SuM (F) and the recording sites in HIP slice (G). EGFP expressed in SuM-DG terminals at normal (left: scale bar, 200 μm) and high (right: scale bar, 50 μm) magnification in acute brain slice (H). After CNO treatment, mEPSCs in GCs [(I) 17 cells from three mice per group], action potentials in GCs [(J) 11 cells from four mice per group], and mEPSCs in CA3 PNs [(K) 9 cells from three mice per group] were recorded. SI test was performed in mice at P42 30 min after CNO intraperitoneal injection [(L) 14 male mice per genotype]. (**M** to **O**) Activation of DG-projecting SuM neurons rescued the impaired DG-CA3 transmission and social recognition. The mEPSCs were recorded in CA3 PNs; 9 to 15 cells from three to six mice per group (M). Diagram of virus injection in DG and SuM at P21 (N). SI test was performed 30 min after CNO injection in mice at P42; 13 to 17 male mice per group (O). Data were shown as means ± SEM. Two-tailed Student's *t* test. $^{**}P < 0.01$ and $^{***}P < 0.001$.

(LENT), and medial entorhinal cortex (MENT; fig. S6B). We noted that the neurons in SuM instead of LENT or MENT were activated in both *Auts2*$^{fl/fl}$ mice and *Auts2*$^{fl/fl;Emx1\text{-}Cre}$ mice after SI (Fig. 6E and fig. S6B).

The SuM-DG axon terminals showed no obvious difference between the two genotypes (fig. S6C). To determine whether the inhibition of SuM-DG circuit would affect DG-CA3 synaptic transmission and social recognition behavior, we inhibited the neuronal activity in this circuit by using the hM4Di-mediated chemogenetic approach (Fig. 6, F to I, and fig. S6, D and E). We then found that the excitability of GCs and DG-CA3 synaptic transmission were significantly reduced (Fig. 6, J and K), and the impaired social recognition was observed (Fig. 6L) in mice with hM4Di expressed in DG-projecting SuM neurons after CNO administration. Furthermore, activation of SuM-DG circuit by hM3Dq overexpression (fig. S6, F and G) remarkably restored the impaired mEPSC frequency in CA3 PNs of *Auts2*$^{fl/fl;Emx1\text{-}Cre}$ mice (Fig. 6M). The rescue effect could be blocked by (2S,2'R,3'R)-2-(2',3'-Dicarboxycyclopropyl) glycine (DCG-IV), which targeted the presynaptic mGluR in the DG-CA3 terminals as an agonist (Fig. 6M), indicating that the rescue effect was due to the facilitation of DG-CA3 synaptic transmission. The social recognition deficit could also be restored after CNO administration (Fig. 6, N and O). These results indicated that modulation of the neuronal activity in SuM-DG circuit could regulate DG-CA3 synaptic transmission. The insufficient neurotransmission in SuM-DG-CA3 circuit caused by DG hypoplasia might be the underlying mechanism of abnormal social recognition behavior in *Auts2*-deleted mice.

Optical modulation of the activity in SuM-DG circuit during encoding phase regulates social recognition memory

We further conducted the fiber photometry to investigate the natural activities of DG-projecting SuM neurons labeled with genetically encoded calcium indicator protein 6 (GCaMP6) protein (Fig. 7A and fig. S7, A to C). Only the Ca^{2+} signals recorded when the subject mice closely interacted with S1 or EM cage (S2) in stage 1 (stage 2) were analyzed (Fig. 7B). We found a significantly robust increase in Ca^{2+} signal that was usually elicited when subject mice investigating the novel S1 mice in contrast to EM cage in stage 1 (Fig. 7C), while almost identical moderate Ca^{2+} transients were observed when they closely interacted with S1 and S2 in stage 2 (Fig. 7D). These results further confirmed that the DG-projecting SuM neurons were involved in the social behavior.

To clarify the detailed phases in which SuM-DG circuit was involved in social recognition behavior, we activated and inhibited the SuM-DG terminals with channelrhodopsin-2 (ChR2) and enhanced natronomonas pharaonis halorhodopsin (eNpHR) overexpression via the delivery of 473-nm blue light and 590-nm yellow light, respectively (Fig. 7E). The efficacies of activation and inhibition were separately assessed by recording the optically evoked action potentials (Fig. 7F) and membrane potential change (Fig. 7G) in SuM neurons. We found that constant illumination of the SuM-DG terminals with yellow light when the subject wild-type mice closely interacted with S1 mice in stage 1 rather than stage 2 showed significantly impaired social novelty recognition (Fig. 7H and fig. S7D). However, wild-type mice with inhibition of the SuM-DG terminals appeared normal object recognition behavior when they closely approached the object in stage 1 (fig. S7E). In addition, optical activation of SuM-DG terminals in wild-type mice in stage 1 facilitated the preference to S2 over S1 in stage 2 in a modified three-chamber SI test (Fig. 7I), although no effect was observed in regular SI test (fig. S7, F to H). Activation of the SuM-DG terminals in *Auts2*$^{fl/fl;Emx1\text{-}Cre}$ mice when they closely interacted with S1 in stage 1 also restored their preference for S2 over S1 in stage 2 (Fig. 7, J and K). These results indicated that optical modulation of the SuM-DG circuit during memory encoding phase could sufficiently regulate social recognition behavior.

DISCUSSION

Many types of NDDs, including ASDs, are marked by a dysfunctional DG (*33*). However, the involvement of related genetic factors in early postnatal development of the DG and relevant autism-like behaviors is not fully understood. A recent study reported that impaired IPC migration and DG hypoplasia were observed in mice with deletion of all major Auts2 isoforms (*34*), which was consistent with our findings. However, we identified a specific developmental phenotype of the HIP with hypoplastic DG in the presence of a normal CA region in our mouse models, in which Auts2 full-length isoform was disrupted due to exon 6 deletion, while Aust2 C-terminal isoforms were intact according to previous research studies (*27*, *34*), indicating that Auts2 full-length isoform might be necessary for the postnatal DG development. In addition, we demonstrated that the first postnatal week was vital for Auts2-mediated DG development, which was closely related to its function in NSC/IPC migration. Deletion of Auts2 beyond this critical period (i.e., *CaMKII*-driven *Auts2* disruption) could not interfere with the morphological and behavioral phenotypes, suggesting the time-sensitive role of Auts2 in the postnatal DG development and related behaviors. Our results provided evidence that genetically modified mouse mutants could be very powerful in linking developmental phenotypes to comprehensive ASD-like behaviors, mimicking the clinical features observed in patients with autism.

Social recognition and memory play important roles in maintaining social groups and interpersonal communication. Multiple recent studies have revealed that the hippocampal subregions including dorsal CA2, ventral CA1, and CA3 are involved in social memory (*35*–*43*). However, the roles of DG, the primary input gateway of the HIP, and DG-related upstream neural circuits in social recognition behavior have not been fully understood (*44*). In the present study, ASD-related core behaviors including SI were assessed in multiple mouse lines with *Auts2* deletion, which strongly suggested a close association between postnatal DG hypoplasia and social recognition deficit. In addition, the reduced DG-CA3 synaptic transmission caused by DG hypoplasia was demonstrated as a target for the recovery of social recognition deficit. Combined with the previous findings that the role of CA3 was important for social memory encoding and retrieval (*42*, *43*), these results would benefit us to understand the involvement of abnormal development and dysfunction of DG-CA3 circuit in social recognition deficit.

As one of the first-order inputs, SuM neurons project to the DG and CA2 of the HIP (*45*). A recent study reported that the SuM-DG and SuM-CA2 circuits were preferentially activated by contextual and social novelty, respectively (*41*). However, another study demonstrated that the anterior DG (aDG)–aCA2/CA3-aCA1 and aDG-aCA2/CA3–posterior CA1 circuits were responsible for the discrimination of nonsocial and social stimuli, respectively (*46*), indicating that multiple intrahippocampal circuits were involved in social recognition. Previous studies have reported that SuM-DG neural transmission could facilitate the network excitability of GCs (*47*, *48*) and regulate

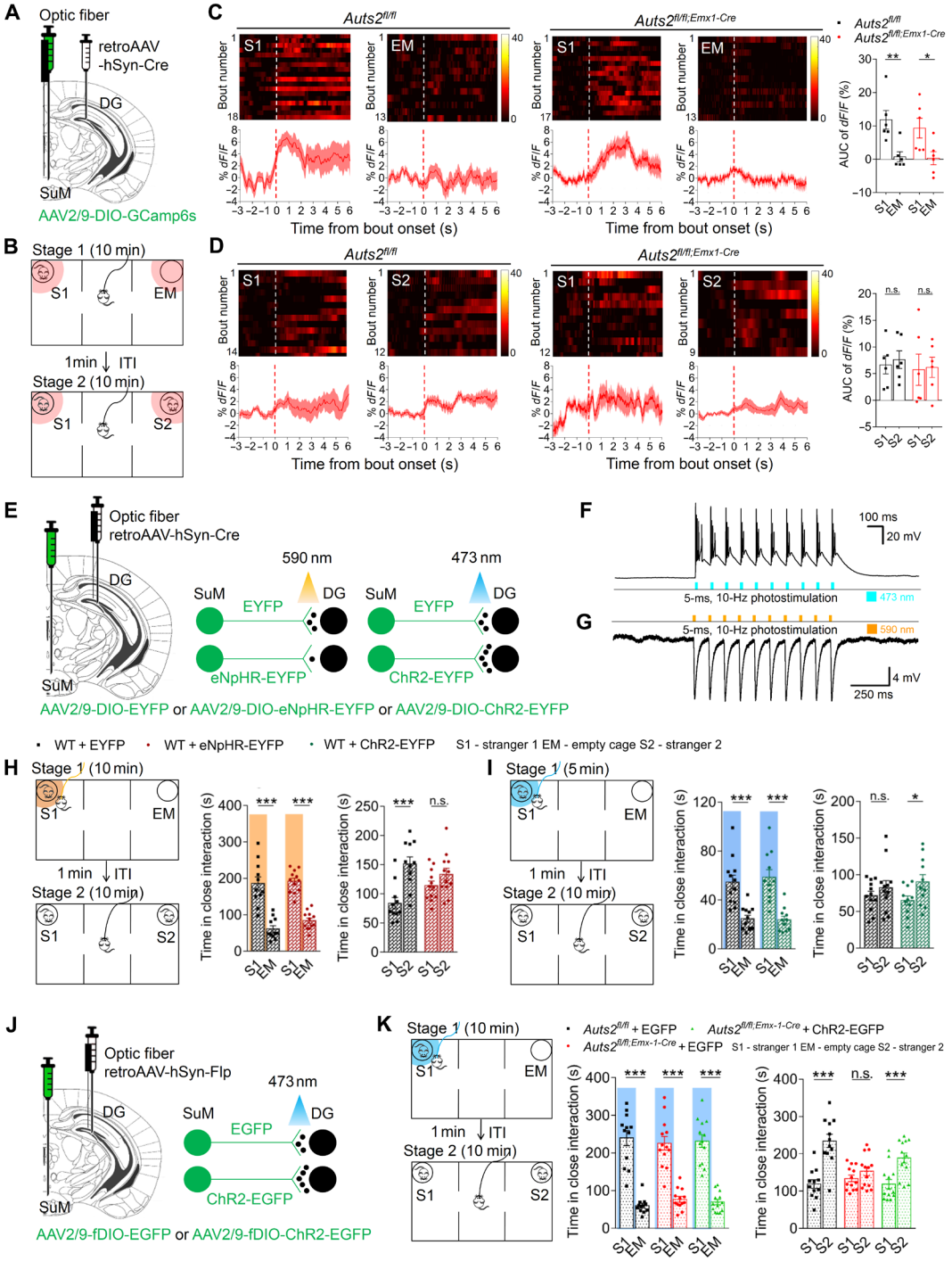

Fig. 7. Optical modulation of the activity in SuM-DG circuit during encoding phase regulates social recognition memory. (**A** to **D**) Schematic diagrams of virus injection in DG and SuM (A) and the fiber photometry recording region during the three-chamber SI test (B). The Ca^{2+} signals in DG-projecting SuM neurons were assessed. Heatmaps (top) and *dF/F* curve (bottom) of averaged GCaMP6s event showed the neuronal response in mice when they closely interacted with S1, S2, and EM in stage 1 (C) and stage 2 (D). Quantitative analysis of area under curve (AUC) of *dF/F* curves; six male mice per genotype. (**E**) Schematic diagram of virus injection in DG and SuM in optogenetic test. Optical activation or inhibition of SuM-DG terminals was performed via the delivery of 473-nm blue light or 590-nm yellow light through bilaterally implanted optic fibers above the DG. WT, wild type. (**F** and **G**) The optically evoked action potentials (F) and membrane potential change (G) were recorded in ChR2 and eNpHR overexpressed SuM neurons via photostimulation for 5 ms at 10 Hz. (**H**) Optical inhibition of SuM-DG terminals only when the subject mice closely interacted with S1 in stage 1 led to social recognition deficit; 11 to12 male mice per group. (**I**) Optical activation of SuM-DG terminals in subject mice during their close interaction with S1 in stage 1 increased the preference for S2 over S1 in a modified SI test in which stage 1 was reduced to 5 min; 11 to 12 male mice per group. (**J** and **K**) Optical activation of SuM-DG terminals with 473-nm blue light pulses in DG (J) of the subject mice during their close interaction with S1 in stage 1 reversed social recognition deficits in male *Auts2*$^{fl/fl;\,Emx1\text{-}Cre}$ mice; 12 to 13 male mice per group (K). Data were shown as means ± SEM. Two-tailed Student's *t* test. **P* < 0.05, ***P* < 0.01, and ****P* < 0.001.

hippocampal θ oscillation (*45*), which was considered as an electrophysiological marker for short-term memory encoding (*49*). In accordance with studies on the role of SuM-DG circuit in integrating GC signals input from other first-order regions (*47*, *48*), we found that the SuM-DG neural circuit was activated in the social recognition behavior, and modulation of this circuit affected the excitability of GCs and DG-CA3 synaptic transmission. By contrary, the inhibition of SuM-DG neural circuit led to social recognition deficit, which might be due to its roles in down-regulating GC activity and inhibiting θ oscillation–dependent encoding of short-term social memory in DG-CA3 neural circuit. However, as the functional monosynaptic inputs from GCs to CA2 PNs have been demonstrated (*50*), the possibility that the DG-CA2 circuit was involved in social recognition cannot be completely excluded. The involvement of SuM-DG circuit in hippocampal encoding for distinguishing similar social information was needed to be investigated in the future.

Moreover, our findings provided the possibility that behaviors could be improved by modulating the neuronal activity in specific neural circuits if the abnormal neurodevelopment resulted from diverse genetic etiologies shared convergent mechanisms in these circuits, although the genetic heterogeneity exists among different individuals. These preclinical evidences might provide new insights in future clinical treatment targeting the specific brain region and neural circuit through noninvasive neuromodulation approaches based on monitoring of neuronal activity in the functioning brain. However, the specific brain area, neural cell types, and circuits should be identified for targeting, and the effect of abnormal neurodevelopment on the structural, especially the functional changes in certain neural circuits, such as the circuit connectivity, neuronal activity, and synaptic transmission, should be clarified.

Previous research studies have reported that Auts2 was a transcriptional activation modulator that acts through the PRC1-P300 signaling pathway during early embryonic brain development (*26*) and critical for the neocortex and DG neurogenesis by regulating RNA metabolism *(34)*. In the present study, we identified that Auts2 interacted with Ctip2, which further facilitated the repressive effect of Ctip2 on Ptgds transcription by recruiting the NuRD repressive transcription complex in normal postnatal DG development. Thus, it was possible that Auts2 had multiple roles in RNA transcription and regulation, and the primary function of Auts2 might be diverse at different neurodevelopmental stages in distinct brain areas. Although the colocalization of Auts2 with Ctip2 was demonstrated in the embryonic neocortex (*27*), the lamellar arrangement of $Ctip2^+$ layer V cortical neurons showed normal in $Auts2^{fl/fl;Emx1\text{-}Cre}$ mice. However, the dysfunction of corticostriatal circuit had been identified in excessive stereotyped behavior (*51*, *52*). As one of the main projection neuronal types in corticostriatal circuit (*53*), the potential dysfunction of $Ctip2^+$ layer V neurons in $Auts2^{fl/fl;Emx1\text{-}Cre}$ and $Auts2^{fl/fl;Nex\text{-}Cre}$ mice might be involved in increased stereotyped behavior, which was worth investigating in the future.

In addition, our results showed that *Auts2* deletion led to ectopic up-regulation of Ptgds, resulting in deficits in NSC/IPC migration and impaired SGZ formation. Ptgds was known as a prostaglandin D synthase in brain that catalyzed the conversion of prostaglandin H2 to prostaglandin D2, which acted as a neuromodulator and/or trophic factor in the central nervous system (*54*). A previous study reported that multiple exposures of sevoflurane-induced neuronal migration deficit in embryonic neocortex were due to the elevated Ptgds expression level (*55*), which also supported our results to a certain extent. Here, we preliminarily identified the role of Ptgds in regulating NSC/IPC migration. Nevertheless, future experiments should be performed to elucidate the mechanism by which Ptgds regulates DG development.

In summary, our study highlighted the vital role of Auts2-related signaling as the transcriptional repressor in the structural and functional development of the postnatal DG. Moreover, SuM-DG-CA3 neurotransmission–dependent social recognition behavior was affected by DG hypoplasia. Our findings might provide new insight into the developmental and neural circuit mechanisms of social dysfunction in patients with *AUTS2* variants.

MATERIALS AND METHODS

Mouse subjects

$Auts2^{fl/fl}$ mice were generated by Biocytogen (Beijing, China). The targeting vector includes the 5′ homology arm (9.4 kb), the 5′ loxP site, and the fragment containing Auts2 exon 6, a neomycin resistance cassette flanked by flippase recombinase target sites, the 3′ loxP site, and the 3′ homology arm (4.1 kb). Clones were analyzed by polymerase chain reaction (PCR) and Southern blotting (probe 1 for the 5′ end and probe 2 for the 3′ end). In the wild-type Auts2 locus, probe 1 hybridized to a 14.1-kb fragment and to a 12.2-kb fragment in the Auts2 loxP allele. Probe 2 hybridized to an 11.5-kb fragment in the wild-type or to a 5.2-kb fragment in the Auts2 loxP allele. Then, the neomycin resistance cassette was removed by crossing with Flipase (Flp) recombinase transgenic mice. Mice homozygous for Auts2 alleles ($Auts2^{fl/fl}$) were crossed with mice expressing the Cre recombinase transgene under the control of the *Emx1*, *Nex*, *Pomc*, or *CaMKII* promoter. The *Emx1*-Cre, *Nex*-Cre, *Pomc*-Cre, and *CaMKII*-Cre mice were gifts from C. Zhao (Southeast University, Nanjing, China), Z. Qiu (Institution of Neuroscience, Chinese Academy of Sciences, Shanghai, China), M. Luo (National Institute of Biological Sciences, Beijing, China), and Y. Ding (Tongji University, Shanghai, China), respectively. All mouse strains used in the present study are on C57BL/6 background. All animal procedures were approved by the Animal Ethical Committee of Peking University Health Center.

Mouse genotyping

The transgenic mice were genotyped by PCR as follows. For $Auts2^{fl/fl}$ mice, the oligos included forward primer 5′-TCCTCGTTTGAATTGACCGGTG-3′ and reverse primer 5′-TGGTTTATGGCTCTAACGCCGTG-3′. The PCR program included 95°C for 5 min (1 cycle); 95°C for 30 s, 59°C for 30 s, and 72°C for 45 s (35 cycles); and 72°C for 10 min (1 cycle); the PCR products were 194 base pairs (bp; wild-type allele) and 323 bp (LoxP allele). For Cre recombinase identification, the PCR product was 499 bp by using the forward primer 5′-CCGCAGAACCTGAAGATG-3′ and reverse primer 5′-GCTACACCAGAGACGGAA-3′ following the same PCR program.

In situ hybridization

Following the previously described procedures (*56*), mice were deeply anesthetized with sodium pentobarbital (40 mg/kg body weight) and were perfused intracardially with 4% (w/v) paraformaldehyde (PFA) in a phosphate-buffered saline (PBS) [137 mM NaCl, 2.7 mM KCl, 4.3 mM Na_2HPO_4, and 1.4 mM KH_2PO_4 (pH 7.4)]. Brains were removed, postfixed overnight in the same fixative at 4°C, and cryoprotected by immersion in 30% (w/v) sucrose

for 2 to 4 days. Then, brains were embedded in optimum cutting temperature compound, sectioned at a thickness of 25 μm on a cryostat, and used for in situ hybridization (ISH) using standard methods. ISH labeling of brain sections was performed with a digoxigenin-labeled Auts2 antisense riboprobe complementary to the mouse Auts2 mRNA (NM_177047.3). Sequences of primers used for ISH probe preparation were 5′-ACTGACACACAGGGATCTGATG-3′ and 5′-CCGTGTGAGTGTCCTTAAATCA-3′. A sense riboprobe was used as a negative control. All hybridizations were performed on sections from at least two separate mice brains at different developmental stages. Sense control showed no signal. ISH signals were imaged using an Olympus IX-71 microscope under bright-field illumination.

Western blotting

Tissues were homogenized with radioimmunoprecipitation assay lysis buffer [50 mM tris (pH 7.4), 150 mM NaCl, 1% Triton X-100, and 0.1% SDS] supplemented with protease inhibitors (Roche, 11697498001). Lysates were centrifuged at 12,000*g* for 20 min. The supernatants were collected and boiled with 4× Laemmli sample buffer (Sigma-Aldrich) and loaded onto 6 to 10% SDS–polyacrylamide gel electrophoresis gels (Invitrogen). After transmembrane, the membranes were blocked at room temperature for 60 min in 5% nonfat drymilk in phosphate-buffered saline Tween (PBST) and then incubated with primary antibodies overnight: rabbit anti-Auts2 (1:1000; Sigma-Aldrich, HPA000390), rabbit anti-Gapdh (1:3000; Cell Signaling Technology, 5174), and goat anti-Ptgds (1:200; Sigma-Aldrich, SAB2502046). After washing with PBST for three times, the horseradish peroxidase–conjugated secondary antibodies (1:2000; Cell Signaling Technology) were incubated at room temperature for 1 hour. Membranes were developed and imaged using an enhanced chemiluminescence reagent (Thermo Fisher Scientific) and a Tanon 5200 Automatic chemiluminescence imaging analysis system (Tanon, Shanghai, China).

Nissl staining

Sections were mounted on microscope slides; air dried; immersed in 0.1% thionin; washed with water; dehydrated in 70, 95, and 100% ethanol for several minutes; and cleared twice in xylene for 5 min. The slides were subsequently covered with mounting medium and mounted with coverslips.

Immunohistochemistry

Sections were washed in PBS, blocked with 5% calf serum, permeabilized in PBST for 1 hour, and incubated in primary antibody diluted in blocking solution overnight at 4°C. Sections were subsequently washed in PBST, incubated in the secondary antibody for 1 hour at room temperature, and washed with PBS three times. As a last step, the slides were covered with mounting medium and mounted with coverslips. The following antibodies and reagents were used for immunostaining: rabbit anti-Cux1 (1:200; Santa Cruz Biotechnology, sc-13024); rat anti-Ctip2 (1:500; Abcam, AB18465); rabbit anti-Foxp2 (1:1000; Sigma-Aldrich, HPA000382); rabbit anti-Tbr1 (1:1000; Abcam, ab31940); rabbit anti-BLBP (1:1000; Abcam, AB32423); rabbit anti-Tbr2 (1:200; Abcam, AB183991); rabbit anti-calretinin (Swant, 7697); mouse anti-NeuN (1:100; Millipore, MAB377B); rabbit anti-GFAP (1:500; Millipore, NE1015-100ULCN); rabbit anti-Ki67 (1:500; Abcam, AB15580); rabbit anti–Ki67–Alexa Fluor 488–conjugated (1:200; Cell Signaling Technology, 11882); rabbit anti–caspase-3 (1:500; Cell Signaling Technology, 9661); rabbit anti-Prox1 (1:100; Millipore, MAB5654); rabbit anti-calbindin (Swant, CB-38a); rabbit anti–c-Fos (1:1000; Novus, NBP2-50057); Alexa Fluor 555 donkey anti-mouse immunoglobulin G (IgG) (1:500; Invitrogen, A31570); Alexa Fluor 633 goat anti-mouse IgG (1:500; Invitrogen, A21050); Alexa Fluor 488/633 goat anti-rabbit IgG (1:500; Invitrogen, A11008/A21071); Alexa Fluor 555 donkey anti-rabbit IgG (1:500; Invitrogen, A31572); and Alexa Fluor 488 goat anti-rat IgG (1:500; Invitrogen, A11006). Hoechst 33342 (1:2000; Invitrogen, H3570) was used for nuclei staining.

EdU labeling

For embryonic cell migration analysis, E12.5, E14.5, and E16.5 pregnant mice were intraperitoneally injected with a 50 μg/g body weight dose of 5-ethynyl-2′-deoxyuridine (Edu) (Invitrogen), and the neonatal mice were harvested at P0 for cell migration analysis. For cell proliferation and cell cycle exit analysis, mice were intraperitoneally injected with a 50 μg/g body weight dose of EdU and then anesthetized and perfused with 4% PFA 4 and 24 hours later, respectively. Frozen sections for the visualization of EdU-labeled cells were reacted by the Click-iT Plus EdU Kit (Invitrogen, C10640) with Alexa Fluor 647 azide for 30 min.

Cell counting

For cell counting, 25-μm coronal hippocampal sections were examined in two to three comparative sections from the anterior to posterior levels in each brain by an experimenter blind to the animal genotype. The pictures used in cell counting were captured using FV1200 confocal microscopy (Olympus, Japan). Pictures were acquired with the 10× or 20× objective lens, and cells were counted in a minimum of three sections taken from each brain. To define the counting area, we used Image-Pro Plus software (Media Cybernetics, USA) to outline the region of interest containing the DG area (including the hilus, granular layer, and molecular layer) manually based on the Hoechst 33342 staining.

Gene expression microarray

Total RNA was extracted from P4 DG tissue with TRIzol (Invitrogen, Carlsbad, CA) according to the manufacturer's protocols. The purity and concentration of RNA were determined from optical density (OD) at 260/280-nm readings using a spectrophotometer (NanoDrop ND-1000). RNA integrity was determined by 1% formaldehyde denaturing gel electrophoresis. Affymetrix GeneChip microarray (Affymetrix Inc., Santa Clara, CA, USA) and Agilentmetrix GeneChip microarray (Agilent Technologies, Santa Clara, CA, USA) were used. Hybridization, data capture, and analysis were performed by CapitalBio Corporation (Beijing, China) according to the manufacturer's protocols. For Affymetrix, total RNA was used for cDNA synthesis, and biotin-tagged cRNA with GeneChip IVT Labeling kit was produced (Affymetrix). The fragmented cRNA with control oligo B2 and eukaryotic hybridization controls was hybridized to each GeneChip array at 45°C for 16 hours (Affymetrix GeneChip Hybridization Oven 640). After hybridization, the GeneChip arrays were washed and then stained with streptavidin phycoerythrinonan with Affymetrix Fluidics Station 450 followed by scanning with the Affymetrix GeneChip Scanner 3000 7G. For Agilentmetrix, cDNA labeled with a fluorescent dye (Cy5 or Cy3-dCTP) was produced by Eberwine's linear RNA amplification method and subsequent enzymatic reaction. The amplified cRNA was purified using the RNA Clean-up Kit (Macherey-Nagel, Germany). Hybridization was performed in a

Agilent Hybridization Oven overnight at a rotation speed of 20 rpm and a temperature of 42°C and washed with two consecutive solutions [0.2% SDS, 2× saline sodium citrate (SSC) at 42°C for 5 min, and 0.2× SSC for 5 min at room temperature]. The hybridization data of Affymetrix were analyzed for normalization and quality control by using the Affymetrix GeneChip Command Console Software and Microarray Suite version 5.0. The threshold values of ≥1.5- and ≤−1.5-fold change were used to select the differentially expressed genes. While GeneSpring software version 13.0 (Agilent) was selected for analysis of the data of Agilentmetrix GeneChip microarray and the threshold of ≥2- and ≤2-fold change and a *t* test *P* vlaue of 0.05 were used to select the differentially expressed genes. The data was $\log_2$-transformed and median-centered by genes using the Adjust Data function of Cluster 3.0 software and then further analyzed with hierarchical clustering with average linkage.

RNAscope

For mRNA detection by using RNAscope, P4 and P14 brains were perfused and fixed in fresh 4% PFA at 4°C for 24 hours, then dehydrated with sucrose solution, and embedded in paraffin. Sections were cut to a thickness of 30 μm, and staining was performed with an RNAscope Multiplex Fluorescent kit (Advanced Cell Diagnostics, 323110, USA), RNAscope 2.5 HD Detection Reagent-RED (Advanced Cell Diagnostics, 322350, USA), and RNAscope 2.5 HD Detection Reagent-BROWN (Advanced Cell Diagnostics, 322310, USA) according to the manufacturer's instructions. Ptgds probe for RNAscope Multiplex Fluorescent assay was designed and synthesized by Advanced Cell Diagnostics.

Quantitative real-time PCR

Total RNA from control and mutant DGs was isolated using the RNeasy Plus Mini Kit for RNA isolation (Qiagen, 74104) according to the manufacturer's instructions, and each sample was reverse-transcribed using a FastKing reverse transcriptase kit (Tiangen, KR116-02). The quantitative PCR reactions were performed using the LightCycler 96 System (Roche). Primers were designed and synthesized as follows: Auts2 primer, 5′-ATCCCGCAGGGAGCACGTA-3′ (forward) and 5′-GGGGAACGGTGTGAAGGTA-3′ (reverse); Ptgds primer, 5′-GAGTACGCTCTGCTATTCAGC-3′ (forward) and 5′-GGTTGGGGCAGGAAAACAATG-3′ (reverse); β-actin primer, 5′-GGCTGTATTCCCCTCCATCG-3′ (forward) and 5′-CCAGTTGGTAACAATGCCATGT-3′ (reverse). The relative gene expression between samples was normalized with the endogenous gene (β-actin).

Cell culture

Human embryonic kidney (HEK) 293 cells were maintained in Dulbecco's Modified Eagle Medium (DMEM) containing 10% fetal bovine serum (FBS), and the expression plasmid [plasmid containing cytomegalovirus-enhancer chicken beta-actin promoter (pcAGGS)-AUTS2–hemagglutinin (HA)–intrinsic ribosomal entry site (IRES)–EGFP, pcDNA3.1-CTIP2-FLAG, or pcDNA3.1-MTA1-Myc] was transfected alone or cotransfected with Lipofectamine 2000 reagent (Invitrogen, 11668) according to manufacturer's instructions. After 6 hours, the medium was changed to fresh DMEM containing 10% FBS and cultured for 48 hours.

Coimmunoprecipitation

For coimmunoprecipitation, the nuclear protein was extracted by using NE-PER Nuclear and Cytoplasmic Extraction Reagents (Thermo Fisher Scientific, 78833) supplemented with protease inhibitor mixture (Roche, 11697498001) and phosphatase inhibitor mixture (Roche, 4906837001) according to the manufacturer's instructions. The overexpressed AUTS2-HA, CTIP2-FLAG, and MTA1-Myc proteins were immunoprecipitated with rabbit anti-HA (Sigma-Aldrich, H9658), mouse anti-FLAG (Sigma-Aldrich, F1804), or rabbit anti-Myc (Sigma-Aldrich, C3956) primary antibodies conjugated to Dynabeads Protein G (Thermo Fisher Scientific, 10003D, USA), respectively. The proteins in the immunoprecipitate were immunoblotted with the same antibodies. For the coimmunoprecipitation of the truncated CTIP2-FLAG with FL-AUTS2-HA or the truncated AUTS2-HA with FL-CTIP2-FLAG, the proteins were immunoprecipitated with the anti-HA antibody and immunoblotted with the anti-HA and anti-FLAG antibodies. The endogenous Ctip2 protein was immunoprecipitated with rat anti-Ctip2 (Abcam, AB18465) primary antibody conjugated to Dynabeads Protein G, and mouse Auts2 and Mta1 were detected with the rabbit anti-Auts2 (1:1000; Sigma-Aldrich, HPA000390) and rabbit anti-Mta1 (1:500; Cell Signaling Technology, D17G10) primary antibodies, respectively.

Dual luminescence assay

The 1.5-kb regulatory sequence containing pretranscriptional start site of PTGDS was subcloned into the Secrete-Pair dual luciferase reporter plasmid. The HEK293T cells cultured in 12-well plates were transfected with plasmids containing AUTS2-HA, CTIP2-FLAG, alone or both of them with the pEZX-PG04-*PTGDS* promoter Gaussia Luciferase/Secreted Alkaline Phosphatase plasmid (GeneCopoeia, CS-HPRM30881-PG04) using Lipofectamine 2000 (Invitrogen, 11668) according to the manufacturer's recommendations. Medium was collected after 48 hours, and the luciferase promoter activity was measured using the Secrete-Pair Dual Luminescence Assay Kit (GeneCopoeia, LF031, Rockville, MD, USA) in a Synergy H1 Hybrid Microplate Reader (Biotek, VT, USA). Gaussia luciferase activity was determined in the supernatant of HEK293T cells by using the activity of secreted alkaline phosphatase as an internal control.

ChIP assay

ChIP was performed using the EZ-ChIP Kit (Millipore, 17-371) according to the manufacturer's instructions. Cross-linked sonicated chromatin was equally divided and immunoprecipitated with indicated antibodies. Quantitative PCR was carried out using the LightCycler 96 System (Roche), and the amounts of immunoprecipitated DNA were normalized to the input. The enrichment of the DNA template was analyzed by conventional PCR or quantitative real-time PCR using primers specific to Ptgds promoter. The sources of the antibodies were rat anti-Ctip2 (Abcam, AB18465) and rabbit anti-Hdac2 (Cell Signaling Technology, 57156). Gene promoter regions were identified by promoter clones (www.genecopoeia.com). Primers for the promoter regions were as the follows: MusPtgdsPro-S1, 5′-CTTCTCCAGCGACCTACT-3′ (forward) and 5′-AGCATCAACCTGTGTGTG-3′ (reverse); MusPtgdsPro-S2, 5′-AGGCAGAGGTTTCTTCTT-3′ (forward) and 5′-ACAAAGCAAGGAAAACTG-3′ (reverse); MusGapdhPro, 5′-CACCATCCGGGTTCCTATAAATAC-3′ (forward) and 5′-CAGCATCCCTAGACCCGTACA-3′ (reverse).

Virus injection and optic fiber implantation

The mice were randomly allocated to different experimental groups. The mouse was anesthetized with an intraperitoneal injection of

pentobarbital sodium (70 mg/kg of body weight), and its head was placed in a stereotactic apparatus. A small craniotomy was performed, and the virus was delivered using a 5-μl syringe with a thin 34-gauge metal needle (Hamilton Instruments) (*56*). For injection of AAV2/9-DIO-Ptgds-2A-EGFP or vehicle in the DG of *Nex*-Cre mice at P3, virus was microinjected into one site in the DG region (0.5 μl per site) on the left and right HIP [anterior-posterior (AP), −1.0 mm; medio-lateral (ML), ± 0.8 mm; dorsoventral (DV), 1.4 mm from the bregma]. For injection of AAV2/9-CaMKII-EGFP-2A-Cre or vehicle in the DG of *Auts2*$^{fl/fl}$ mice, or AAV2/9-CaMKII-hM4Di-mCherry or vehicle in the DG of wild-type mice at P14, virus was microinjected into two sites in the DG region (0.5 μl per site) on the left and right HIP (site 1: AP, −1.3 mm; ML, ± 1.4 mm; DV, 1.8 mm from the bregma; site 2: AP, −2.3 mm; ML, ±2.2 mm; DV, 2.0 mm from the bregma). For whole-cell electrophysiology, hSyn-hM3Dq or DIO (fDIO)-hM3Dq/hM4Di/ChR2/eNpHR-expression AAV was microinjected in SuM (AP, −2.2 mm; ML, ± 0 mm; DV, 4.7 mm from the bregma, 1.0 μl per site), accompanied by Cre (Flp)–expression retroAAV microinjection in DG region on the left and right HIP (AP, −2.0 mm; ML, ± 1.5 mm; DV, 1.9 mm from the bregma) at P14 to P17. For fiber photometry, chemogenetic, or optogenetic behavioral tests, DIO (fDIO)–hM3Dq/hM4Di/ChR2/eNpHR/GCaMP6-expression AAV was microinjected in SuM (AP, 2.6 mm; ML, ± 0 mm; DV, 4.8 mm from the bregma), accompanied by Cre (Flp)–expression retroAAV microinjection in DG region on the left and right HIP (AP, 2.5 mm; ML, ± 1.7 mm; DV, 2.0 mm from the bregma) at P21 to P24, and the optic fiber was implanted in DG or SuM 0.3 mm above the virus injection site at P35 to P38. The flow rate (0.05 μl/min) was controlled by an injection pump (KD Scientific, USA). After injection, the needle was left in place for an additional 5 min and then was withdrawn slowly.

MCPG intracerebroventricular injection

Mice were anesthetized, and two cannulae (length, 1 cm; outer diameter, 0.8 mm; internal diameter, 0.5 mm) were placed bilaterally at P35. The stereotactic coordinates for the CA3 region of the HIP were 2.8 mm (AP), 2.6 mm (ML), and 3.0 mm (DV) from the Bregma. After 1 week of recovery, MCPG with the dosage of 10 mg was diluted in 0.48 ml of NaOH (110 mM) to obtain the 100 mM MCPG solution. MCPG (1 μmol per mouse) or vehicle (110 mM NaOH) was administered intracerebroventricularly 15 min before the beginning of three-chamber SI test in a volume of 10 μl at the rate 1 μl/10 s. The injection needle remained in place for additional 30 s before removal.

Intraperitoneal CNO administration

For the chemogenetic experiment, CNO (Tocris Bioscience, 4936, USA) was initially dissolved in dimethyl sulfoxide (DMSO; 10 mg/ml) and then diluted with saline (5% DMSO). Animals were treated with CNO at the dose of 3 mg/kg by intraperitoneal injection. CNO was administrated 30 min before the sacrifice in electrophysiological recording or behavioral tests.

Whole-cell electrophysiology and data analysis

Mice were anesthetized with isoflurane and then decapitated. The brains were quickly removed and sliced on a vibratome (Leica VT1200S, Wetzlar, Germany) in ice-cold cutting solution consisting of 213 mM sucrose, 3 mM KCl, 26 mM $NaHCO_3$, 1 mM NaH_2PO_4, 5 mM $MgCl_2$, 0.5 mM $CaCl_2$, and 10 mM glucose (adjusted to pH 7.3 to 7.4, 300 to 310 mOsm, saturated with 95% O_2 and 5% CO_2). The slices were incubated for 30 min at 37°C, maintained at room temperature (24° to 25°C) in a solution consisting of 125 mM NaCl, 5 mM KCl, 26 mM $NaHCO_3$, 2 mM NaH_2PO_4, 1.3 mM $MgCl_2$, 2.6 mM $CaCl_2$, and 10 mM glucose, and then recovered for 30 min before recording. Whole-cell patch-clamp recordings were performed in neurons from the SuM, GCs from the DG, and PNs from the CA3 regions by using 3- to 6-megaohm borosilicate glass pipettes (World Precision Instruments) pulled with a Brown-Flaming micropipette puller (P-97; Sutter Instruments Company). The recording pipettes were filled with the internal solution consisting of 145 mM KCl, 5 mM NaCl, 10 mM Hepes, 5 mM EGTA, 4 mM MgATP, and 0.3 mM Na_2GTP (pH 7.25 with KOH, 300 to 310 mOsm). For action potential recording, spikes were induced by current injection from −50 to 250 pA for 400 ms in 50-pA increments. The mEPSCs and mIPSCs recordings were obtained in voltage-clamped at −60 mV in a bath containing 1 μM tetrodotoxin and 100 μM picrotoxin for mEPSCs or 1 μM tetrodotoxin, 10 μM cyanquixaline, and 50 μM D-AP5 for mIPSCs. The mEPSC/mIPSC amplitude and frequency were determined in a 5-min time window for three to five times. Evoked EPSCs were pharmacologically isolated by 100 μM picrotoxin (PTX) in bath by stimuli (30 μA, 0.3 ms) through a concentric bipolar electrode (CE2C75; FH-Co. Inc) with an isolated pulse stimulator (Master-8 and ISO-Flex, A.M.P. Instruments, LTD). Paired-pulse ratios of evoked EPSCs in CA3 region were tested with intervals of 10, 20, 50, 100, 200, 300, 600, and 1000 ms. Current-clamp recordings were obtained from GFP/mCherry-expressing neurons to identify membrane potential/action potential or mEPSC changes upon chemogentic or optogenetic stimulation. For hM3Dq or hM4Di expression neurons in SuM or DG, the mice were injected with the AAV at P14, and CNO with the dose of 3 mg/kg was intraperitoneally injected 30 min before the sacrifice at P28. For the slices from mice with hM3Dq or hM4Di expression in SuM, an incision was made between CA2 and CA3 before the action potential or mEPSCs recorded in neurons of DG or CA3. For ChR2 or eNpHR expression neurons in SuM, the mice were injected with the AAV at P14 and sacrificed at P35, a blue/yellow light (473/590 nm, 10 mW, 5 ms width with 10 pulses at 10 Hz) was delivered to ChR2/eNpHR-expressing neurons in the SuM region via an optic fiber attached to a laser. The data were digitized at 10 kHz with a 2.9-kHz low-pass filter. The membrane capacitance, series resistance, and holding current were determined from the pCLAMP 10 during recording. The recorded cells with series resistances of >30 megaohm were rejected. All data were recorded using MultiClamp 700B amplifier and pCLAMP 10.6 software and were then analyzed by Clampfit 10.6 (Molecular Devices) and Igor 6.22 (WaveMetrics) software.

Three-chamber SI test

According to the previous study *(56)*, 6- to 7-week-old male or female animals were used across all tests. Target subjects (S1 and S2) were 6- to 7-week old gender matched mice that had been habituated by being placed inside the grid enclosure for 3 days before the beginning of testing. The social testing arena was a white rectangular, three-chambered box. Each chamber was 20 cm by 40 cm by 22 cm in size. Dividing walls were made from Plexiglas, with rectangular openings (5 cm by 8 cm), allowing access into each chamber. The chambers of the arena were cleaned by ethanol between trials. Test mice were habituated to the testing room for at least 30 min before

the start of behavioral tasks. The enclosures have an internal diameter of 7 cm and a height of 15 cm; the grid bars are 5 mm in diameter and are 10 mm apart, allowing nose contact through the bars but preventing fighting. During a 5-min habituation period, the test mouse was placed in the middle chamber, the sliding doors were opened, and the mouse was given free access to the entire arena. Each of the two outside chambers contained a grid enclosure. The mouse was recognized by the EthoVision 7.0 video tracking system (Nodules). The amount of time spent in each chamber and the number of entries into each chamber were recorded. After the habituation period, an unfamiliar mouse (S1) that had had no prior contact with the test mouse was placed in one of the enclosures. The sliding doors were opened, and the test mouse was allowed to explore the entire social test arena for a 10-min session. The amount of time spent in each chamber and the time spent in close interaction (with the nose point within 2 cm of the enclosure) were recorded. Beginning 1 min after the end of the first 10-min session, each mouse was tested in a second 10-min session to quantify social preference for a different stranger. Another unfamiliar mouse (S2) was placed into the previously empty enclosure. The test mouse had a choice between the first, already-investigated mouse (familiar S1) and the novel, unfamiliar mouse (new S2). As described above, the amount of time spent in each chamber and the time spent in close interaction during the second 10-min session were recorded and analyzed.

Four-trial social memory assay in the three-chamber apparatus

As in the sociability and social novelty preference assays in the three-chamber apparatus, a 6- to 7-week-old male mouse was placed in the middle chamber after a 5-min habituation period and was allowed SI with an unfamiliar mouse (S1), which was placed in either the left or right grid enclosure for a 10-min trial. After the initial session, the subject mouse was allowed two additional successive 1-min trials of SI with the familiar mouse (S1). On the fourth trial, the S1 mouse was replaced by a novel stimulus mouse (S2), and the test mouse was allowed another 10-min trial. The percentage of time spent in close interaction with the stranger was calculated as the time of close interaction with S1/2 divided by total time spent in close interaction with S1/2 and the empty cage (*56*).

Ultrasonic voice

Each pup was isolated from its dam and littermates and was placed in a small enclosure with a soft plastic surface in a soundproof chamber (temperature, 25° ± 1°C). Audio recordings lasted 5 min and were conducted every 3 days on P3, P6, and P9. Recording hardware (Avisoft UltraSound Gate 116 Hm with a high-quality condenser microphone) and software (Avisoft SASLab Pro Recorder) were from Avisoft Bioacoustics (sampling frequency, 300 kHz; fast Fourier transform length, 1024 points; 16-bit format). Both male and female pups were used (*57*).

Stereotypic behaviors

After 10-min habituation, male or female mice in their home cages with fresh bedding were used to measure the time spent in repetitive behaviors including grooming and digging during the next 10 min (*56*). Grooming behavior was defined as stroking or scratching of face, head, or body with the two forelimbs or licking body parts. Digging behavior was defined as the behavior in which a mouse coordinately uses two fore legs or hind legs to dig out or displace bedding materials.

Olfactory habituation/dishabituation test

The test was performed as described previously (*56*). Each test session was conducted in a clean mouse cage containing fresh litter. Odor stimulants were delivered with a cotton-tipped swab through a hole in the center of the cage top positioned 7 cm above the bedding. After 2 min of habituation to a cotton-tipped swab without odor stimulant, subjects were tested individually for the time spent sniffing cotton-tipped swabs. The olfactory cues were designed to present familiar and unfamiliar odors, with and without social valence. Sequences of three identical swabs assayed habituation to the same smell. Switching to different smells on the swabs assayed dishabituation, i.e., recognition that an odor is new. Swabs were dipped in (i) tap water, (ii) almond extract (1:100 dilution; McCormick), (iii) urine of an unfamiliar mouse of the same strain and sex, and (iv) urine of another unfamiliar mouse of the same strain and sex. The order of swab presentation was water, water, water, almond, almond, almond, unfamiliar urine 1, unfamiliar urine 1, unfamiliar urine 1, unfamiliar urine 2, unfamiliar urine 2, and unfamiliar urine 2. The time spent sniffing the swab was quantitated with a stopwatch by an observer uninformed about the genotype of the subject mouse. Sniffing was scored when the mouse's nose was within 2 cm of the cotton swab. Each swab was presented for a 2-min period, with a 1-min interval following the last swab presentation, for a total session length of ~40 min per mouse.

Novel object recognition assay

Following the previously described procedures (*56*), the object recognition test was performed in an open field apparatus [40 cm (length) by 40 cm (width) by 40 cm (height)]. During the sample phase, the mouse was allowed to explore two identical objects for 20 min. The test phase, in which one of the two objects was replaced with a new one, was performed 1 min later, and the time spent exploring each of the two objects during the next 10 min was measured. Object exploration was defined as each instance in which a mouse's nose touched the object or was oriented toward the object and came within 2 cm of it.

Y-maze

A black Y-shape maze (40 cm by 5 cm each arm) was used with overall illumination at ~200 lux. Mice were placed into the center of arms faced to any one arm (A-B-C in order) and allowed to freely explore for 10 min. This arm was designated as a start arm. Arm entry was defined as entry of the whole body into an arm. We recorded the sequence of arm entries every time. The percentage of accurate spontaneous alternations was calculated (*57*).

Morris water maze assay

As previously described (*56*), the Morris water maze consisted of a circular white plastic tank 120 cm in diameter filed with water (21° to 22°C) containing nontoxic titanium white pigment to obscure the submerged platform. After habituation, male mice were trained to find an unmarked and submerged hidden platform (10 cm in diameter) for consecutive five training days. Mice were given four trials per day. At the start of each trial, the mouse was placed gently into the water with its head facing the wall of the pool. The start location varied semirandomly between trials (four different

starting locations spaced evenly around the pool). If a mouse did not find the platform within 1 min, then it was placed on the platform by the experimenter, kept there for 15 s, and then was removed to a warmed home cage. Training was performed for seven consecutive days, and the latency to the platform was evaluated by EthoVision 8.0 program (Noldus).The probe test with the platform removed from the pool was given for 1 min on day 8 (24 hours after the last training session). The percentage of time spent in the four quadrants of the pool and the swimming speed were recorded.

Contextual fear conditioning and extinction

The test was following the previously described procedures (*56*). After habituation, the mouse was placed in the box and allowed to explore freely for 2 min before receiving five foot shocks (0.8 mA, 2 s) with intershock intervals of 2 min (Med Associates). The mouse was returned to its home cage 2 min after the final foot shock. Freezing behavior was measured as the amount of time the mouse exhibited freezing behavior during each intershock interval. To study the extinction of contextual fear memory, the mouse was placed in the conditioned fear context 24 hours after fear conditioning, and its contextual freezing behavior was measured for 30 min (5 min per block for six blocks) without the administration of any foot shock.

Open field assay

We used a clear Plexiglas box [27.5 cm (length) by 27.5 cm (width) by 20 cm (height); Med Associates] for the open field assay. Mice were placed in the center of the chamber at the beginning of the assay. The distance traveled within 60 min (six blocks, 10 min for each block) and the time spent in the central and peripheral zones of the open field for first 10 min were recorded as indices of anxiety-like behaviors (*56*).

Dark/light box test

The test was performed in the open field with a dark box insert apparatus [27.5 cm (length) by × 27.5 cm (width) by 20 cm (height); Med Associates] with one side (the dark chamber) draped in black cloth and the other (the light chamber) illuminated at ~50 lux with a high-intensity house light. Mice were habituated in an adjacent room to low-light conditions (~5 lux), and the test room initially was under similar illumination. The mouse was placed in the dark chamber, the light chamber was illuminated, and the door between the two chambers was opened. The mouse was allowed to explore the apparatus freely for 5 min. The percentage of time spent in the illuminated chamber was used as indices of anxiety-like behaviors *(56)*.

Elevated plus maze test

The test was performed by using an elevated plus maze made of gray Perspex with a central 5 cm–by–5 cm central platform, two open arms of 30 cm by 5 cm, and two enclosed arms of 30 cm by 5 cm by 15 cm, elevated to a height of 60 cm above the floor. Individual animals were placed on the central platform facing an open arm of the plus maze. Behavior was recorded for 5 min by an overhead video camera and a computer equipped with the EthoVision 8.0 video tracking system (Nodules) to calculate the time each animal spent in the open or closed arms. The proportion of time spent in open arms was used for the estimation of anxiety-like behaviors (*56*).

Prepulse inhibition test

According to the previous study (*56*), a startle reflex measurement system (MED Associate) was used in the prepulse inhibition test. A male mouse was placed in a Plexiglas cylinder where it was left undisturbed for 3 min. White noise at a level of 66 dB lasting 40 ms was used as the startle stimulus for all trial types. The startle response was recorded for 300 ms (measuring the response every 1 ms) starting with the onset of the prepulse stimulus. The peak startle amplitude recorded during the 180-ms sampling window was used as the dependent variable. A test session consisted of four trial types (i.e., one type for startle stimulus only trials, and three types for prepulse inhibition trials). The intensity of startle stimulus was 110 dB. The prepulse sound was presented 120 ms before the startle stimulus, and its intensity was 70, 74, or 82 dB. Three combinations of prepulse and startle stimuli were used: 70 to 110 dB, 74 to 110 dB, and 82 to 110 dB. The average ITI was 15 s (range, 7 to 23 s). Four blocks of the four trial types were presented in pseudorandom order so that each trial type was presented once within a block.

Fiber photometry recording

The mice with the injection of retroAAV-hSyn-Cre in the ventral DG and AAV2/9-EF1a-DIO-GCaMP6s in the SuM were used for fiber photometry. An optic fiber was implanted above the SuM. Fiber photometry experiments were performed at least 3 weeks after GCaMP6s injection in SuM. The start of fiber photometry of Ca^{2+} signals was 1 week after implantation surgery. To record the Ca^{2+} fluorescent signals, a laser beam from a 488-nm laser (OBIS 488LS, Coherent) was reflected by a dichroic mirror (MD498, Thorlabs), focused by an objective lens [10×; numerical aperture (NA), 0.3; Olympus), and then coupled to an optical commutator (Doric Lenses). An optical fiber (OD, 200 mm; NA, 0.37; 1.5 m long) coupled the light between the commutator and the implanted optical fiber. GCaMP6 fluorescent signals were collected by the same fiber and objective, then band-pass–filtered (MF525-39, Thorlabs), and detected by a photomultiplier tube (R3896, Hamamatsu). An amplifier (C7319, Hamamatsu) converted the photomultiplier tube current output to a voltage signal, which was further filtered through a low-pass filter (35-Hz cutoff; Brownlee, 440). The analog voltage signals were digitalized at 500 Hz and recorded by fiber photometry software (Thinkerbiotech, Nanjing, China). The excitation light with the intensity of 40 to 50 μW was used, and the gain was adjusted to a level that gave a background signal of 4 to 5 units measured when the end of the input cable was in the dark. Fiber photometry recording data were exported to custom-written MATLAB software for further analysis. The fluorescence change (dF/F) was calculated as $(F - F0)/F0$, where $F0$ is the baseline fluorescence signal. Events were identified as the peak that exceeded the mean by 1 SD. The area under the curve was calculated as mean $\Delta F/F$ of the event.

Optogenetics

The mice with the injection of retroAAV-hSyn-Cre in the ventral DG and AAV2/9-EF1a-DIO-ChR2/eNpHR-EYFP in the SuM were used for optogenetics. An optic fiber was implanted above the ventral DG. The experiments were performed at least 3 weeks after the virus injection and 1 week after implantation surgery. For optogenetics, the dividing walls of three-chamber were made from Plexiglas with rectangular openings (15 cm by 22 cm), allowing

access into each chamber. Behavior-triggered activation experiments were performed. The target zone for light stimulation was determined by a circle centered on the enclosures with a radius of 14 cm (two times the holders' radius). In S1 versus empty session, only during the ON phases, when the nose point of test mice entered the target zone, a transistor-transistor logic (TTL) signal triggered the stimulus generator. The signal from the stimulus generator activated the lasers through a controller (Hong Kong Plexon). The blue (473 nm) light and yellow (590 nm) light (10 mW, 5 ms width with 10 pulses at 10 Hz) were delivered to the ends of the optic fiber for ChR2 activation and eNpHR inhibition, respectively.

Statistical analysis

During testing and scoring, the experimenters were blinded to the genotype of the mice. Samples size (n) was indicated in the figure legends and in data S2, which are based on our previous works and those commonly used in the field. The statistical removal of outliers was performed in the cells of electrophysiological experiments. No samples or animals were excluded unless specified in the experimental procedure. All data in accordance with the normal distribution were represented as means ± SEM. The homogeneity test of variance was performed before the statistical test. Statistical Package for the Social Sciences 20.0 (Chicago, IL, USA) and GraphPad Prism 7.04 were used for statistical analysis and drawing of statistical charts, respectively. The details of the statistical methods and results were summarized in data S2. A P value of less than 0.05 was considered as statistical significance.

SUPPLEMENTARY MATERIALS

Supplementary material for this article is available at https://science.org/doi/10.1126/sciadv.abk1238

View/request a protocol for this paper from *Bio-protocol*.

REFERENCES AND NOTES

1. M. Fernandez, I. Mollinedo-Gajate, O. Penagarikano, Neural circuits for social cognition: Implications for autism. *Neuroscience* **370**, 148–162 (2018).
2. S. Weigelt, K. Koldewyn, N. Kanwisher, Face identity recognition in autism spectrum disorders: A review of behavioral studies. *Neurosci. Biobehav. Rev.* **36**, 1060–1084 (2012).
3. X. Jiang, A. Bollich, P. Cox, E. Hyder, J. James, S. A. Gowani, N. Hadjikhani, V. Blanz, D. S. Manoach, J. J. S. Barton, W. D. Gaillard, M. Riesenhuber, A quantitative link between face discrimination deficits and neuronal selectivity for faces in autism. *NeuroImage Clin.* **2**, 320–331 (2013).
4. J. Tang, M. Falkmer, C. Horlin, T. Tan, S. Vaz, T. Falkmer, Face recognition and visual search strategies in autism spectrum disorders: Amending and extending a recent review by Weigelt et al. *PLOS ONE* **10**, e0134439 (2015).
5. S. N. Rigby, B. M. Stoesz, L. S. Jakobson, Empathy and face processing in adults with and without autism spectrum disorder. *Autism Res.* **11**, 942–955 (2018).
6. N. J. Sasson, R. B. Nowlin, A. E. Pinkham, Social cognition, social skill, and the broad autism phenotype. *Autism* **17**, 655–667 (2013).
7. D. W. Halliday, S. W. MacDonald, K. S. Scherf, J. W. Tanaka, A reciprocal model of face recognition and autistic traits: Evidence from an individual differences perspective. *PLOS ONE* **9**, e94013 (2014).
8. G. J. Lewis, N. G. Shakeshaft, R. Plomin, Face identity recognition and the social difficulties component of the autism-like phenotype: Evidence for phenotypic and genetic links. *J. Autism Dev. Disord.* **48**, 2758–2765 (2018).
9. T. Iidaka, S. Terashima, K. Yamashita, T. Okada, N. Sadato, Y. Yonekura, Dissociable neural responses in the hippocampus to the retrieval of facial identity and emotion: An event-related fMRI study. *Hippocampus* **13**, 429–436 (2003).
10. M. J. Taylor, T. Mills, E. W. Pang, The development of face recognition; hippocampal and frontal lobe contributions determined with MEG. *Brain Topogr.* **24**, 261–270 (2011).
11. R. K. Olsen, Y. Lee, J. Kube, R. S. Rosenbaum, C. L. Grady, M. Moscovitch, J. D. Ryan, The role of relational binding in item memory: Evidence from face recognition in a case of developmental amnesia. *J. Neurosci.* **35**, 5342–5350 (2015).
12. E. Ji, C. S. Weickert, R. Lenroot, J. Kindler, A. J. Skilleter, A. Vercammen, C. White, R. E. Gur, T. W. Weickert, Adjunctive selective estrogen receptor modulator increases neural activity in the hippocampus and inferior frontal gyrus during emotional face recognition in schizophrenia. *Transl. Psychiatry* **6**, e795 (2016).
13. E. H. Aylward, N. J. Minshew, G. Goldstein, N. A. Honeycutt, A. M. Augustine, K. O. Yates, P. E. Barta, G. D. Pearlson, MRI volumes of amygdala and hippocampus in non-mentally retarded autistic adolescents and adults. *Neurology* **53**, 2145–2150 (1999).
14. R. Nicolson, T. J. DeVito, C. N. Vidal, Y. Sui, K. M. Hayashi, D. J. Drost, P. C. Williamson, N. Rajakumar, A. W. Toga, P. M. Thompson, Detection and mapping of hippocampal abnormalities in autism. *Psychiatry Res.* **148**, 11–21 (2006).
15. O. Saitoh, C. M. Karns, E. Courchesne, Development of the hippocampal formation from 2 to 42 years: MRI evidence of smaller area dentata in autism. *Brain* **124**, 1317–1324 (2001).
16. J. Wegiel, I. Kuchna, K. Nowicki, H. Imaki, J. Wegiel, E. Marchi, S. Y. Ma, A. Chauhan, V. Chauhan, T. W. Bobrowicz, M. de Leon, L. A. S. Louis, I. L. Cohen, E. London, W. T. Brown, T. Wisniewski, The neuropathology of autism: Defects of neurogenesis and neuronal migration, and dysplastic changes. *Acta Neuropathol.* **119**, 755–770 (2010).
17. J. Wegiel, N. C. Schanen, E. H. Cook, M. Sigman, W. T. Brown, I. Kuchna, K. Nowicki, J. Wegiel, H. Imaki, S. Y. Ma, E. Marchi, T. Wierzba-Bobrowicz, A. Chauhan, V. Chauhan, I. L. Cohen, E. London, M. Flory, B. Lach, T. Wisniewski, Differences between the pattern of developmental abnormalities in autism associated with duplications 15q11.2-q13 and idiopathic autism. *J. Neuropathol. Exp. Neurol.* **71**, 382–397 (2012).
18. R. Sultana, C.-E. Yu, J. Yu, J. Munson, D. Chen, W. Hua, A. Estes, F. Cortes, F. de la Barra, D. Yu, S. T. Haider, B. J. Trask, E. D. Green, W. H. Raskind, C. M. Disteche, E. Wijsman, G. Dawson, D. R. Storm, G. D. Schellenberg, E. C. Villacres, Identification of a novel gene on chromosome 7q11.2 interrupted by a translocation breakpoint in a pair of autistic twins. *Genomics* **80**, 129–134 (2002).
19. X. L. Huang, Y. S. Zou, T. A. Maher, S. Newton, J. M. Milunsky, A de novo balanced translocation breakpoint truncating the autism susceptibility candidate 2 (AUTS2) gene in a patient with autism. *Am. J. Med. Genet. A* **152A**, 2112–2114 (2010).
20. G. Beunders, S. A. de Munnik, N. van der Aa, B. Ceulemans, E. Voorhoeve, A. J. Groffen, W. M. Nillesen, E. J. Meijers-Heijboer, R. Frank Kooy, H. G. Yntema, E. A. Sistermans, Two male adults with pathogenic AUTS2 variants, including a two-base pair deletion, further delineate the AUTS2 syndrome. *Eur. J. Hum. Genet.* **23**, 803–807 (2015).
21. Y. Fan, W. Qiu, L. Wang, X. Gu, Y. Yu, Exonic deletions of AUTS2 in Chinese patients with developmental delay and intellectual disability. *Am. J. Med. Genet. A* **170A**, 515–522 (2016).
22. G. Beunders, J. van de Kamp, P. Vasudevan, J. Morton, K. Smets, T. Kleefstra, S. A. de Munnik, J. Schuurs-Hoeijmakers, B. Ceulemans, M. Zollino, S. Hoffjan, S. Wieczorek, J. So, L. Mercer, T. Walker, L. Velsher; the DDD study, M. J. Parker, A. C. Magee, B. Elffers, R. F. Kooy, H. G. Yntema, E. J. Meijers-Heijboer, E. A. Sistermans, A detailed clinical analysis of 13 patients with AUTS2 syndrome further delineates the phenotypic spectrum and underscores the behavioural phenotype. *J. Med. Genet.* **53**, 523–532 (2016).
23. S. C. S. Nagamani, A. Erez, B. Ben-Zeev, M. Frydman, S. Winter, R. Zeller, D. El-Khechen, L. Escobar, P. Stankiewicz, A. Patel, S. W. Cheung, Detection of copy-number variation in AUTS2 gene by targeted exonic array CGH in patients with developmental delay and autistic spectrum disorders. *Eur. J. Hum. Genet.* **21**, 343–346 (2013).
24. E. Sengun, K. Yararbas, S. Kasakyan, Y. Alanay, AUTS2 Syndrome in a 68-year-old female: Natural history and further delineation of the phenotype. *Am. J. Med. Genet. A* **170**, 3231–3236 (2016).
25. G. Beunders, E. Voorhoeve, C. Golzio, L. M. Pardo, J. A. Rosenfeld, M. E. Talkowski, I. Simonic, A. C. Lionel, S. Vergult, R. E. Pyatt, J. van de Kamp, A. Nieuwint, M. M. Weiss, P. Rizzu, L. E. N. I. Verwer, R. M. L. van Spaendonk, Y. Shen, B. L. Wu, T. Yu, Y. Yu, C. Chiang, J. F. Gusella, A. M. Lindgren, C. C. Morton, E. van Binsbergen, S. Bulk, E. van Rossem, O. Vanakker, R. Armstrong, S. M. Park, L. Greenhalgh, U. Maye, N. J. Neill, K. M. Abbott, S. Sell, R. Ladda, D. M. Farber, P. I. Bader, T. Cushing, J. M. Drautz, L. Konczal, P. Nash, E. de Los Reyes, M. T. Carter, E. Hopkins, C. R. Marshall, L. R. Osborne, K. W. Gripp, D. L. Thrush, S. Hashimoto, J. M. Gastier-Foster, C. Astbury, B. Ylstra, H. Meijers-Heijboer, D. Posthuma, B. Menten, G. Mortier, S. W. Scherer, E. E. Eichler, S. Girirajan, N. Katsanis, A. J. Groffen, E. A. Sistermans, Exonic deletions in AUTS2 cause a syndromic form of intellectual disability and suggest a critical role for the C terminus. *Am. J. Hum. Genet.* **92**, 210–220 (2013).
26. Z. Gao, P. Lee, J. M. Stafford, M. von Schimmelmann, A. Schaefer, D. Reinberg, An AUTS2-Polycomb complex activates gene expression in the CNS. *Nature* **516**, 349–354 (2014).
27. K. Hori, T. Nagai, W. Shan, A. Sakamoto, S. Taya, R. Hashimoto, T. Hayashi, M. Abe, M. Yamazaki, K. Nakao, T. Nishioka, K. Sakimura, K. Yamada, K. Kaibuchi, M. Hoshino, Cytoskeletal regulation by AUTS2 in neuronal migration and neuritogenesis. *Cell Rep.* **9**, 2166–2179 (2014).
28. K. Yamashiro, K. Hori, E. S. K. Lai, R. Aoki, K. Shimaoka, N. Arimura, S. F. Egusa, A. Sakamoto, M. Abe, K. Sakimura, T. Watanabe, N. Uesaka, M. Kano, M. Hoshino, AUTS2

governs cerebellar development, purkinje cell maturation, motor function and social communication. *iScience* **23**, 101820 (2020).
29. K. Hori, K. Yamashiro, T. Nagai, W. Shan, S. F. Egusa, K. Shimaoka, H. Kuniishi, M. Sekiguchi, Y. Go, S. Tatsumoto, M. Yamada, R. Shiraishi, K. Kanno, S. Miyashita, A. Sakamoto, M. Abe, K. Sakimura, M. Sone, K. Sohya, H. Kunugi, K. Wada, M. Yamada, K. Yamada, M. Hoshino, AUTS2 regulation of synapses for proper synaptic inputs and social communication. *iScience* **23**, 101183 (2020).
30. F. Bedogni, R. D. Hodge, B. R. Nelson, E. A. Frederick, N. Shiba, R. A. Daza, R. F. Hevner, Autism susceptibility candidate 2 (Auts2) encodes a nuclear protein expressed in developing brain regions implicated in autism neuropathology. *Gene Expr. Patterns* **10**, 9–15 (2010).
31. V. B. Cismasiu, K. Adamo, J. Gecewicz, J. Duque, Q. Lin, D. Avram, BCL11B functionally associates with the NuRD complex in T lymphocytes to repress targeted promoter. *Oncogene* **24**, 6753–6764 (2005).
32. R. Simon, H. Brylka, H. Schwegler, S. Venkataramanappa, J. Andratschke, C. Wiegreffe, P. Liu, E. Fuchs, N. A. Jenkins, N. G. Copeland, C. Birchmeier, S. Britsch, A dual function of Bcl11b/Ctip2 in hippocampal neurogenesis. *EMBO J.* **31**, 2922–2936 (2012).
33. H. Hagihara, K. Takao, N. M. Walton, M. Matsumoto, T. Miyakawa, Immature dentate gyrus: An endophenotype of neuropsychiatric disorders. *Neural Plast.* **2013**, 1–24 (2013).
34. A. S. Castanza, S. Ramirez, P. P. Tripathi, R. A. M. Daza, F. K. Kalume, J. M. Ramirez, R. F. Hevner, AUTS2 regulates RNA metabolism and dentate gyrus development in mice. *Cereb. Cortex* **26**, 4808–4824 (2021).
35. F. L. Hitti, S. A. Siegelbaum, The hippocampal CA2 region is essential for social memory. *Nature* **508**, 88–92 (2014).
36. E. L. Stevenson, H. K. Caldwell, Lesions to the CA2 region of the hippocampus impair social memory in mice. *Eur. J. Neurosci.* **40**, 3294–3301 (2014).
37. A. S. Smith, S. K. Williams Avram, A. Cymerblit-Sabba, J. Song, W. S. Young, Targeted activation of the hippocampal CA2 area strongly enhances social memory. *Mol. Psychiatry* **21**, 1137–1144 (2016).
38. A. Oliva, A. Fernandez-Ruiz, F. Leroy, S. A. Siegelbaum, Hippocampal CA2 sharp-wave ripples reactivate and promote social memory. *Nature* **587**, 264–269 (2020).
39. T. Meira, F. Leroy, E. W. Buss, A. Oliva, J. Park, S. A. Siegelbaum, A hippocampal circuit linking dorsal CA2 to ventral CA1 critical for social memory dynamics. *Nat. Commun.* **9**, 4163 (2018).
40. T. Okuyama, T. Kitamura, D. S. Roy, S. Itohara, S. Tonegawa, Ventral CA1 neurons store social memory. *Science* **353**, 1536–1541 (2016).
41. S. Chen, L. He, A. J. Y. Huang, R. Boehringer, V. Robert, M. E. Wintzer, D. Polygalov, A. Z. Weitemier, Y. Tao, M. Gu, S. J. Middleton, K. Namiki, H. Hama, L. Therreau, V. Chevaleyre, H. Hioki, A. Miyawaki, R. A. Piskorowski, T. J. McHugh, A hypothalamic novelty signal modulates hippocampal memory. *Nature* **586**, 270–274 (2020).
42. M. C. Chiang, A. J. Y. Huang, M. E. Wintzer, T. Ohshima, T. J. McHugh, A role for CA3 in social recognition memory. *Behav. Brain Res.* **354**, 22–30 (2018).
43. X.-D. Liu, P.-H. Ai, X.-N. Zhu, Y.-B. Pan, M. M. Halford, M. Henkemeyer, D.-F. Feng, T.-L. Xu, S. Sun, N.-J. Xu, Hippocampal Lnx1-NMDAR multiprotein complex mediates initial social memory. *Mol. Psychiatry* **26**, 3956–3969 (2021).
44. C. Leung, F. Cao, R. Nguyen, K. Joshi, A. J. Aqrabawi, S. Xia, M. A. Cortez, O. C. Snead III, J. C. Kim, Z. Jia, Activation of entorhinal cortical projections to the dentate gyrus underlies social memory retrieval. *Cell Rep.* **23**, 2379–2391 (2018).
45. W. X. Pan, N. McNaughton, The supramammillary area: Its organization, functions and relationship to the hippocampus. *Prog. Neurobiol.* **74**, 127–166 (2004).
46. T. Raam, K. M. McAvoy, A. Besnard, A. H. Veenema, A. Sahay, Hippocampal oxytocin receptors are necessary for discrimination of social stimuli. *Nat. Commun.* **8**, 2001 (2017).
47. K. Nakanishi, H. Saito, K. Abe, The supramammillary nucleus contributes to associative EPSP-spike potentiation in the rat dentate gyrusin vivo. *Eur. J. Neurosci.* **13**, 793–800 (2001).
48. Y. Hashimotodani, F. Karube, Y. Yanagawa, F. Fujiyama, M. Kano, Supramammillary nucleus afferents to the dentate gyrus Co-release glutamate and GABA and potentiate granule cell output. *Cell Rep.* **25**, 2704–2715.e4 (2018).
49. R. P. Vertes, Hippocampal theta rhythm: A tag for short-term memory. *Hippocampus* **15**, 923–935 (2005).
50. K. Kohara, M. Pignatelli, A. J. Rivest, H. Y. Jung, T. Kitamura, J. Suh, D. Frank, K. Kajikawa, N. Mise, Y. Obata, I. R. Wickersham, S. Tonegawa, Cell type-specific genetic and optogenetic tools reveal hippocampal CA2 circuits. *Nat. Neurosci.* **17**, 269–279 (2014).
51. A. E. Abbott, A. C. Linke, A. Nair, A. Jahedi, L. A. Alba, C. L. Keown, I. Fishman, R. A. Müller, Repetitive behaviors in autism are linked to imbalance of corticostriatal connectivity: A functional connectivity MRI study. *Soc. Cogn. Affect. Neurosci.* **13**, 32–42 (2018).
52. A. V. Kalueff, A. M. Stewart, C. Song, K. C. Berridge, A. M. Graybiel, J. C. Fentress, Neurobiology of rodent self-grooming and its value for translational neuroscience. *Nat. Rev. Neurosci.* **17**, 45–59 (2016).
53. Y. Kawaguchi, Pyramidal cell subtypes and their synaptic connections in layer 5 of rat frontal cortex. *Cereb. Cortex* **27**, 5755–5771 (2017).
54. A. Nagata, Y. Suzuki, M. Igarashi, N. Eguchi, H. Toh, Y. Urade, O. Hayaishi, Human brain prostaglandin D synthase has been evolutionarily differentiated from lipophilic-ligand carrier proteins. *Proc. Natl. Acad. Sci. U.S.A.* **88**, 4020–4024 (1991).
55. D. Chai, Y. Cheng, Y. Sun, J. Yan, R. Hu, L. Zhang, H. Jiang, Multiple sevoflurane exposures during pregnancy inhibit neuronal migration by upregulating prostaglandin D2 synthase. *Int. J. Dev. Neurosci.* **78**, 77–82 (2019).
56. J. Li, A. Chai, L. Wang, Y. Ma, Z. Wu, H. Yu, L. Mei, L. Lu, C. Zhang, W. Yue, L. Xu, Y. Rao, D. Zhang, Synaptic P-Rex1 signaling regulates hippocampal long-term depression and autism-like social behavior. *Proc. Natl. Acad. Sci. U.S.A.* **112**, E6964–E6972 (2015).
57. X. Sun, L. Wang, C. Wei, M. Sun, Q. Li, H. Meng, W. Yue, D. Zhang, J. Li, Dysfunction of Trio GEF1 involves in excitatory/inhibitory imbalance and autism-like behaviors through regulation of interneuron migration. *Mol. Psychiatry* , (2021).
58. A. Jolley, M. Corbett, L. McGregor, W. Waters, S. Brown, J. Nicholl, S. Yu, De novo intragenic deletion of the autism susceptibility candidate 2 (AUTS2) gene in a patient with developmental delay: A case report and literature review. *Am. J. Med. Genet. A* **161A**, 1508–1512 (2013).
59. I. E. Amarillo, W. L. Li, X. Li, E. Vilain, S. Kantarci, De novo single exon deletion of AUTS2 in a patient with speech and language disorder: A review of disrupted AUTS2 and further evidence for its role in neurodevelopmental disorders. *Am. J. Med. Genet. A* **164A**, 958–965 (2014).
60. Y. Liu, D. Zhao, R. Dong, X. Yang, Y. Zhang, K. Tammimies, M. Uddin, S. W. Scherer, Z. Gai, De novo exon 1 deletion of AUTS2 gene in a patient with autism spectrum disorder and developmental delay: A case report and a brief literature review. *Am. J. Med. Genet. A* **167**, 1381–1385 (2015).

Acknowledgments: We are thankful to X. Yu for the valuable help in suggesting the experimental design. **Funding:** This work was supported by grants from Key Realm R&D Program of Guangdong Province (2019B030335001), the National Key R&D Program of China (2016YFC1307000), and the National Natural Science Foundation of China (81730037, 81825009, 81871077, 81971283, and 82071541). **Author contributions:** J.L. and D.Z. designed the research. J.L., X.S., Y.Y., Q.L., C.W., L.Z., M.S., H.M., and T.Z. performed the research and analyzed the data. J.L., W.Y., L.W., and D.Z. wrote and refined the article. **Competing interests:** The authors declare that they have no competing interests. **Data and materials availability:** All data needed to evaluate the conclusions in the paper are present in the paper and/or the Supplementary Materials.

Submitted 25 June 2021
Accepted 6 January 2022
Published 2 March 2022
10.1126/sciadv.abk1238